Journal of Fluids and Structures 18 (2003) 665–694

JOURNAL OF
FLUIDS AND
STRUCTURES

www.elsevier.nl/locate/jnlabr/yjfls

Imaging of the self-excited oscillation of flow past a cavity during generation of a flow tone

M. Geveci[a], P. Oshkai[a], D. Rockwell[a,*], J.-C. Lin[a], M. Pollack[b]

[a] *354 Packard Laboratory, Department of Mechanical Engineering and Mechanics, Lehigh University, 19 Memorial Drive West Bethlehem, PA 18015-3085, USA*
[b] *Lockheed-Martin, PO Box 1072, Schenectaby, NY 12301, USA*

Received 24 June 2002; accepted 31 July 2003

Abstract

Flow through a pipeline-cavity system can give rise to pronounced flow tones, even when the inflow boundary layer is fully turbulent. Such tones arise from the coupling between the inherent instability of the shear flow past the cavity and a resonant acoustic mode of the system. A technique of high-image-density particle image velocimetry is employed in conjunction with a special test section, which allows effective laser illumination and digital acquisition of patterns of particle images. This approach leads to patterns of velocity, vorticity, streamline topology and hydrodynamic contributions to the acoustic power integral. Comparison of global, instantaneous images with time- and phase-averaged representations provides insight into the small-scale and large-scale concentrations of vorticity, and their consequences on the topological features of streamline patterns, as well as the streamwise and transverse projections of the hydrodynamic contribution to the acoustic power integral. Furthermore, these global approaches allow the definition of effective wavelengths and phase speeds of the vortical structures, which can lead to guidance for physical models of the dimensionless frequency of oscillation.

---

1. Introduction

1.1. Overview of flow tones

Flow tones are generated in a wide variety of configurations. In essence, they arise due to favorable coupling between an inherent instability of a separated shear layer and a resonant acoustic mode of the flow system. Possible configurations and physical issues associated with tone generation are reviewed by Rockwell and Naudascher (1978, 1979), Rockwell (1983), Blake (1986), Howe (1997, 1998) and Rockwell (1998).

The focus of the present investigation is tone generation due to flow past a cavity. Relevant studies, which have provided considerable insight in recent years, are summarized by Rockwell et al. (2003). They include a jet through a system of orifice plates (Hourigan et al., 1990; Stoubos et al., 1999), a separated shear layer past a cavity resonator (DeMetz and Farabee, 1977; Elder, 1978; Elder et al., 1982; Nelson et al., 1981, 1983), and a separated layer past a resonant side branch in the form of a duct or pipe (Pollack, 1980; Bruggeman et al., 1989, 1991; Kriesels et al., 1995; Ziada and Bühlmann, 1992; Ziada and Shine, 1999).

---

*Corresponding author. Tel.: +1-610-758-4107; fax: 610-758-4041.
E-mail address: dor0@lehigh.edu (D. Rockwell).

0889-9746/$ - see front matter © 2003 Elsevier Ltd. All rights reserved.
doi:10.1016/j.jfluidstructs.2003.07.017

For a given cavity configuration, the occurrence of purely hydrodynamic oscillations involves a number of common elements that are described, for example, by Rockwell (1983) and Blake (1986). In the presence of an acoustic resonator, however, the coexistence of hydrodynamic and acoustic fields influences the predominant mechanisms leading to highly coherent oscillations, as described in the formulation of Howe (1975, 1980).

This investigation addresses the case of an axisymmetric cavity bounded by pipes at either end. A detailed assessment of the pressure fluctuations associated with tone generation in this configuration is given by Rockwell et al. (2003). The emphasis of the current study is on the flow patterns within the cavity. It is therefore appropriate to consider previous investigations that have addressed physical aspects of this class of problems; they are briefly described below.

1.2. Qualitative visualization of flow patterns during generation of tones

Cremer and Ising (1967) visualized the large-amplitude oscillations of a planar jet at the mouth of an organ pipe using a Michelson inferometer. The transverse undulations of the jet were associated with the generation of very large-scale vortical structures in the vicinity of the impingement edge, which appeared to exceed those attainable with a purely hydrodynamic instability. Bruggeman (1987) injected a small amount of CO_2 in an airflow past a side branch, thereby allowing visualization of the transverse undulations of the unstable interface during coupling with an acoustic mode. In related investigations of the same type of configuration during flow tone generation, Ziada (1994) showed, via smoke visualization, the effect of the level of the self-excited acoustic fluctuation on the generation of large-scale vortices. Kriesels et al. (1995) injected small amounts of Neon and Argon in the airflow to visualize further features of the vortex formation and the distortion of its trajectory along the mouth of the cavity due to acoustic resonant coupling. Hourigan et al. (1990) and Huang and Weaver (1991) used smoke to visualize, during the generation of tones, the large-scale vortex generation between two orifice plates located in a pipe. Nelson et al. (1981) used smoke to visualize analogous large-scale vortices along the mouth of the cavity undergoing Helmholtz resonance.

A common feature of all of these visualizations is the rapid onset of large-scale vortices in the separated shear layer. In fact, these patterns can be interpreted in conjunction with an instantaneous pressure signal, in order to qualitatively investigate the role of the vortices during the generation of acoustic power, as shown by Bruggeman (1987), Hourigan et al. (1990), Ziada (1994), and Kriesels et al. (1995). The theoretical framework in all of these investigations is the integral relation for acoustic power formulated by Howe (1975, 1980).

1.3. Pointwise measurement of flow characteristics during generation of tones

A variety of investigations have provided insight into certain features of the unstable shear layer at selected points along the opening of the cavity. Approaches include the use of hot wire and laser Doppler anemometry, which yielded phase- or time-averaged representations of flow quantities. Elder (1978) and Elder et al. (1982) employed hot-wire measurements to determine the unsteady deflection of the wave-like interface along the mouth of a cavity undergoing resonant oscillations in the depthwise mode. Schachenmann and Rockwell (1980) undertook hot wire measurements along the axis of a jet through an axisymmetric cavity at the exhaust of a plenum excited in a Helmholtz resonance mode. A quasi-standing-wave phenomenon through the cavity was characterized; it involved superposition of hydrodynamic and acoustic fluctuations. Rockwell and Schachenmann (1982a, b) considered flow tone generation due to an axisymmetric cavity bounded by a resonant pipe at its upstream side and an orifice at its downstream side. Hot wire measurements were employed to determine the critical values of phase shift along the axis of the cavity that are necessary for self-sustained generation of flow tones. Moreover, Rockwell and Schachenmann (1982a) determined the eigenfunctions of the unsteady shear layer, along with phase maps throughout the shear layer, and corresponding spectral distributions of the velocity fluctuation component. Nelson et al. (1981) used laser Doppler velocimetry to determine the steady and unsteady velocity fields, in addition to patterns of Reynolds stress, in the opening of a cavity resonating in the Helmholtz mode. These data were employed in the theoretical model of Nelson et al. (1983), which focused on the evaluation of the energy production. Zoccola (2000) employed hot wire measurements to characterize the shear layer past a resonant cavity and determined the velocity spectra, velocity–pressure coherence, Reynolds stress, root-mean-square (rms) vorticity and mean energy production, which was interpreted within the theoretical framework of Nelson et al. (1983).

1.4. Discrete and distributed models of the separated shear layer during flow tone generation

Representation of the vortices along the mouth of the cavity has involved discrete (line) vortices, which are shed periodically from the leading-corner of the edge or cavity. This type of vortex model, which assumes the vorticity to be concentrated at a point, has been employed in models of flow tone generation from a flute by Howe (1975) and from a Helmholtz resonator by Nelson et al. (1983). In addition, Bruggeman et al. (1989) also employed a line vortex representation to model resonant oscillations of a shear layer past a side branch. These vortex simulations have proved effective in describing critical features of acoustic power generation according to the integral relationship of Howe (1975, 1980) and energy production according to the model of Nelson et al. (1983).

The evolution of the undulating shear layer leading to the formation of a vortex can be modelled using a distributed representation of vorticity in the form of, for example, a large number of discrete vortices. Hourigan et al. (1990) used this type of vortex sheet representation, whereby the sheet was made up of a large number of vortex clusters in order to simulate the vortex development between two orifice plates during the generation of flow tones. Using a conceptually similar approach, Kriesels et al. (1995) numerically simulated the evolution of the vortex sheet using vortex clusters and obtained good agreement with flow visualization. Further, Hofmans (1998) employed similar simulation for flow tone generation due to a separated shear layer along the mouth of a side branch. Another type of numerical approach, which involves the solution of the compressible Navier–Stokes equations, has been undertaken by Radavich et al. (1999). They considered the vortex development during tone generation for the classic configuration of a side branch. Their simulation accounted for the interaction between the mean flow and the acoustic field, and they presented instantaneous representations of the acoustic power integral due to Howe (1975, 1980), as well as other terms that are associated with local compressibility and viscosity.

1.5. Flow tone generation from a shallow cavity: unresolved issues

The focus of the present investigation is on the flow physics associated with the generation of acoustic tones arising from flow past a shallow axisymmetric cavity. This configuration is distinguished from those described in the foregoing investigations in several respects. For the aforementioned cavities in the form of a side branch or Helmholtz resonator, the depth of the cavity is sufficiently large such that the shear layer develops in an essentially independent fashion along the mouth of the cavity opening. In contrast, for the case of a shallow cavity, the shear layer tends to attach to the cavity floor. This confinement effect may influence the unsteady evolution of the shear layer instability and the associated vortex formation. In essence, the unsteady and averaged flow patterns past a shallow cavity during the generation of tones is not understood.

For the majority of the flow configurations described in the foregoing, especially those that emphasized an understanding of the flow physics through visualization and numerical simulation, the orientation of the resonant acoustic waves is orthogonal to the direction of the inflow. In contrast, for the present configuration, they are nominally aligned, except for distortions within the cavity. This difference is expected to influence the acoustic power generation and thereby the tendency to generate phase-locked flow tones.

The inflow boundary layer in previous investigations of tone generation arising from flow past cavities has ranged from a highly accelerated laminar to a fully turbulent boundary layer. For the latter case, details are lacking on the transformation from a fully turbulent state to coherent oscillations of the shear layer during generation of a flow tone.

The possibility of vortical structures of widely disparate scales in the separated shear layer during the generation of tones has not been addressed. In the event that the vorticity thickness of the separated boundary layer is relatively small, as is the case for a fully turbulent boundary layer at separation, one expects small-scale vortices to be formed from the leading-edge of the cavity, in accord with recent investigations of purely hydrodynamic oscillations of jet-edge (Lin and Rockwell, 2001a) and cavity (Lin and Rockwell, 2001b) configurations with fully-developed turbulent boundary layers at separation. Generation of flow tones may, however, be associated with the formation of a large-scale vortex in the shear layer. The mechanisms by which small-scale vortices develop into larger ones in the shear layer during excitation of an acoustic resonator have not been addressed.

Global, instantaneous representations of the flow patterns associated with flow tone generation have not been pursued. Of particular interest are patterns of both the instantaneous vorticity and the hydrodynamic contribution to the acoustic power integral of Howe (1975, 1980). These types of instantaneous representations, along with others, can provide physical insight into the corresponding phase- or time-averaged representations.

Generation of flow tones is assumed to involve a consistent phase-locking of the flow patterns from cycle to cycle of the flow tone oscillation. This feature has been clearly established for the foregoing configurations. The present situation of tone generation due to flow past a long, shallow cavity bounded by pipes at either end may yield resonant acoustic amplitudes that are relatively small, and thereby an intermittent lock-on of the hydrodynamic field, which would be evident from examination of a succession of instantaneous states.

The overall aim of the present investigation is to clarify the foregoing issues using a technique of high-image-density particle image velocimetry.

2. Experimental system and techniques

The experimental system consisted of two subsystems: the air supply system; and the actual pipe-cavity system.

2.1. Air supply system

The air supply system consisted of an air compressor, a compressed air plenum, and an air dryer-filter unit. All of these components were self-contained in a room that was isolated from the actual experimental facility by a thick ceramic wall, in order to preclude contaminating influences of noise and vibration.

The conditioned air was transmitted through the wall to an arrangement of valves and pressure regulators, which are shown on the left-hand side of the schematics of Fig. 1a. Line *A* was the primary air source for the present experiment. It consisted of two valves and a pressure regulator, which were connected to the inlet of the plenum by a flexible rubber hose. Line *B* was used for extremely low flow rates, which are not part of the present series of investigations. Finally, line *C*, which also included a valve and pressure regulator, provided air to the seed generator.

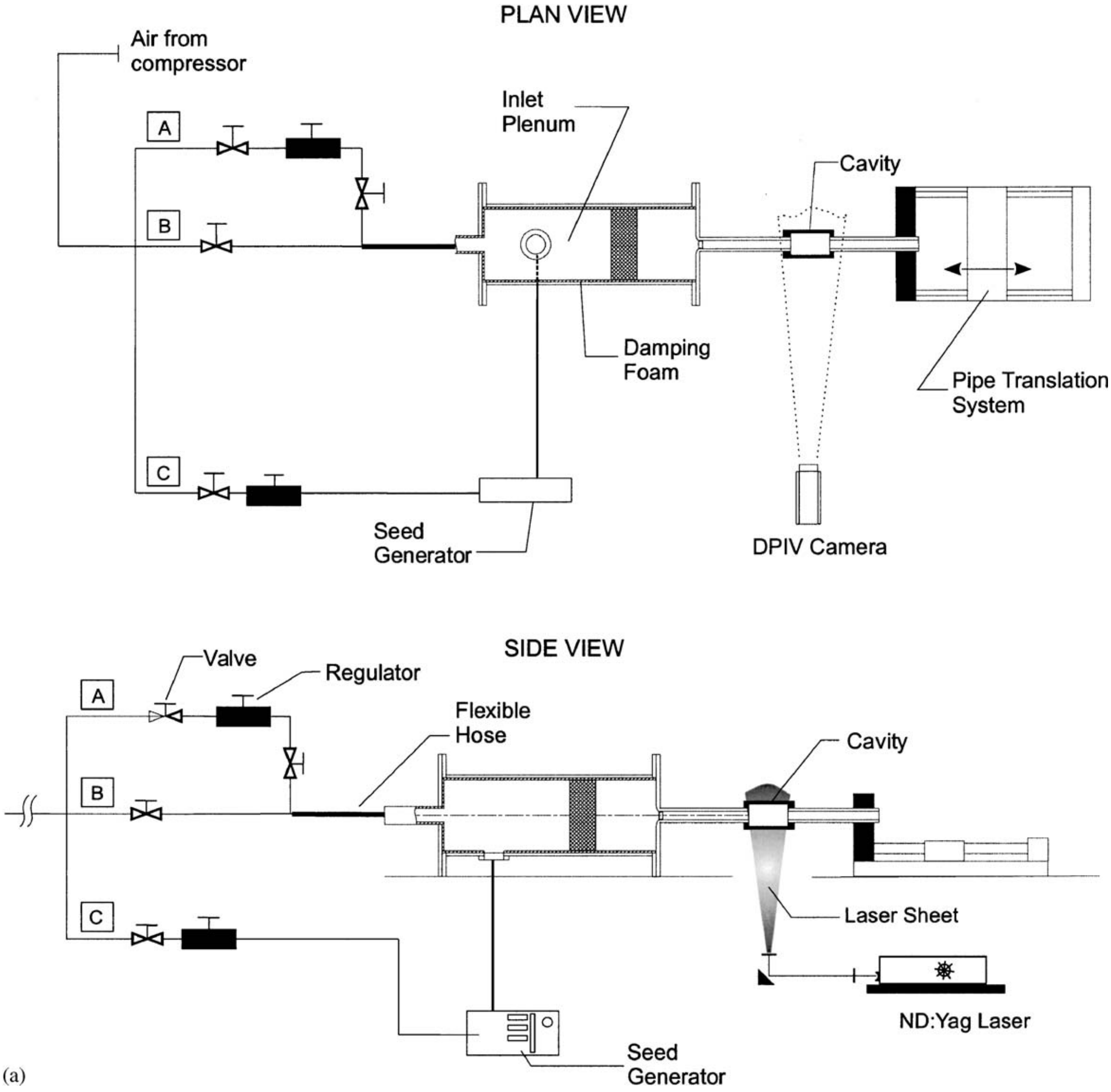

(a)

Fig. 1. (a) Overview of experimental system. (b) Cavity subsystem employed for PIV imaging. (c) Spectra of pressure fluctuations at locations in the inlet pipe (p_a), on the floor of the cavity (p_b) and at the trailing (impingement) corner of the cavity (p_c).

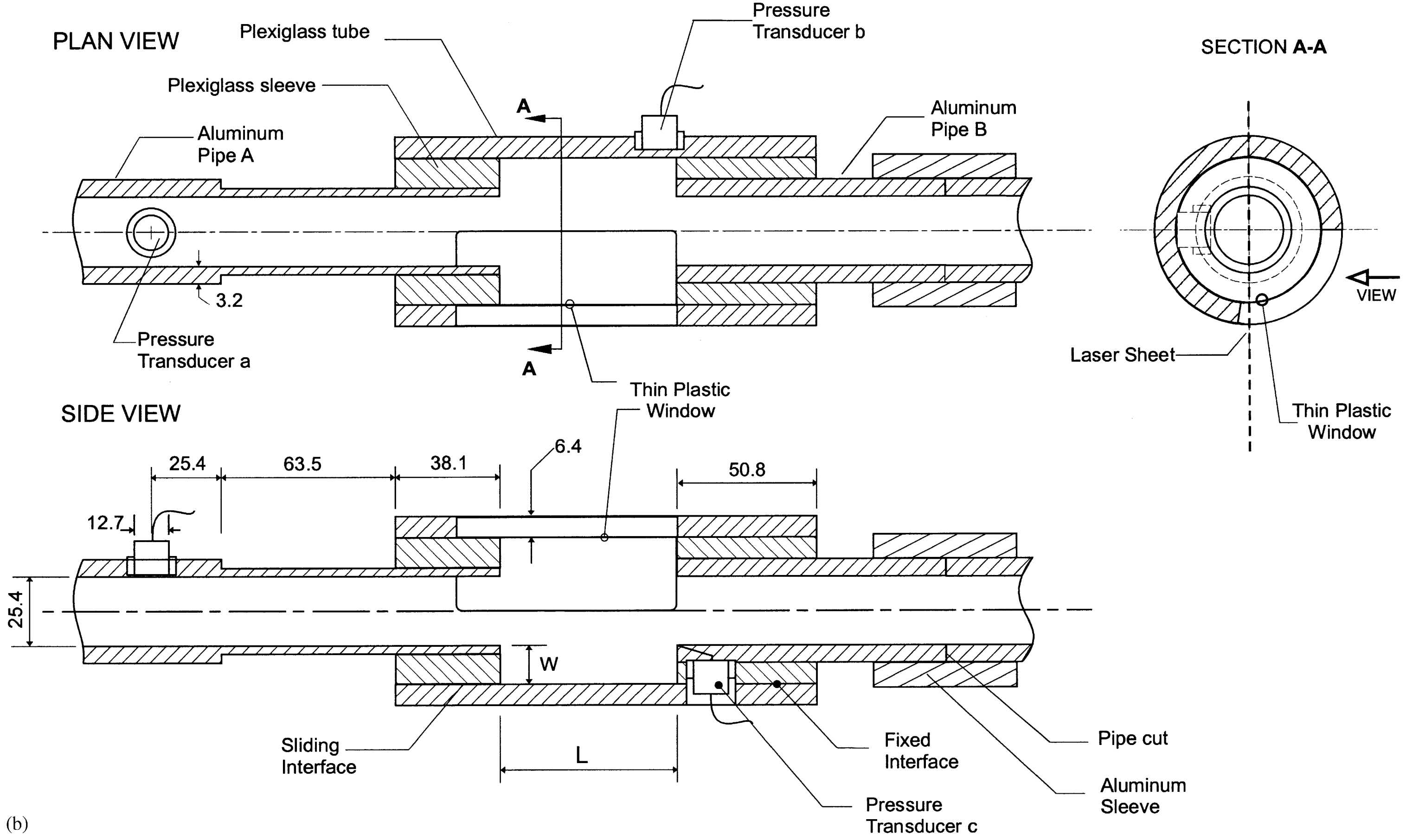

Fig. 1 (*continued*).

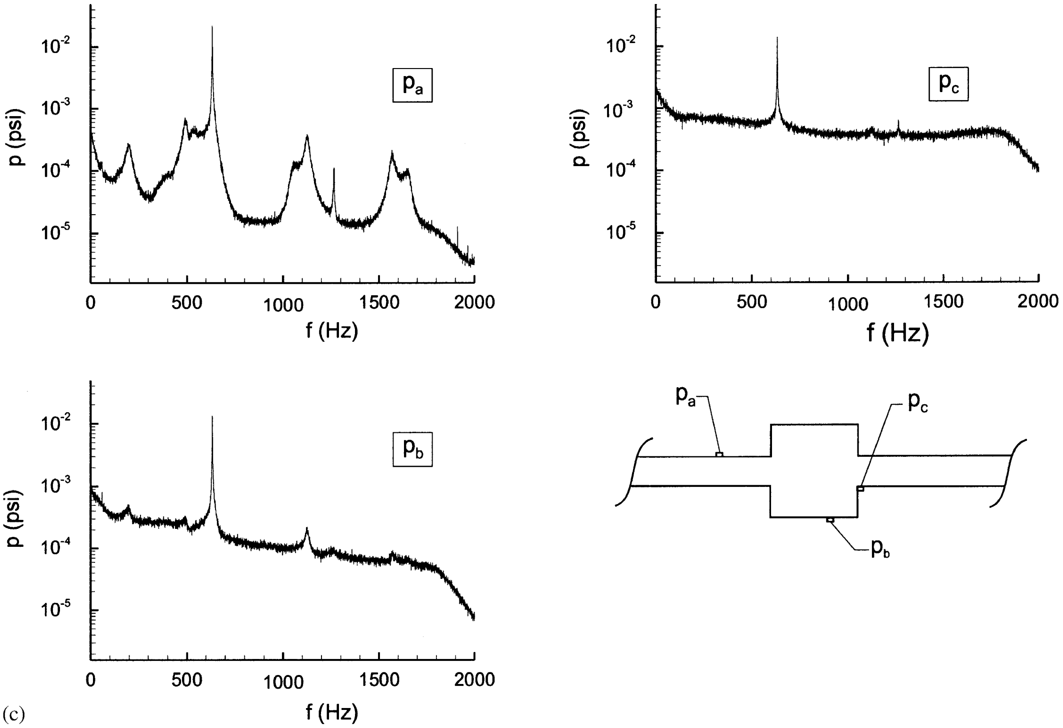

Fig. 1 (*continued*).

The principal components of the pipe-cavity system are shown in the schematics of Fig. 1a. The inlet plenum was of Plexiglas, had a diameter of 203 mm and a length of 61 cm, and housed a honeycomb structure, which acted as a flow straightener. Furthermore, the inside of the plenum was lined with acoustic damping foam, in order to minimize the occurrence of localized acoustic resonance. The exhaust line of the seed generator, which was operated during digital particle image velocimetry (DPIV) measurements, was connected to the plenum in the manner shown in Fig. 1a.

The transformation from the flow within the plenum to the entrance of the pipe-cavity system was accomplished through a contraction located at the exit of the plenum. It was designed with a contour to preclude separation in the pipe inlet. A roughened ring with a height of 1 mm and a streamwise length of 4 mm was located immediately downstream of the pipe inlet. It ensured that the flow at the pipe inlet was adequately tripped, in order to optimize the generation of a fully turbulent boundary layer at the cavity inlet, as verified in the independent hot wire experiments of Rockwell et al. (2003). At the exit of the inlet pipe, i.e., the entrance of the cavity, the momentum thickness θ_0 relative to the pipe diameter was $\theta_0/D = 0.016$. Furthermore, measurements of streamwise turbulence intensity u_{rms} within the boundary layer showed a peak magnitude and location characteristic of a turbulent boundary layer, as discussed in detail by Rockwell et al. (2003).

The pipeline-cavity arrangement consisted of a 30.48 cm inlet (upstream) pipe, the cavity subsystem and a 30.48 cm exhaust (downstream) pipe. The aluminum inlet and exhaust pipes were of 25.4 mm internal diameter.

Multiple pressure transducers were located along the inlet and exhaust pipes. For the purpose of the present investigation, which requires a well-defined reference pressure signal during the acquisition of images, the pressure transducer at a location of 127 mm upstream of the exit of the inlet pipe was employed for all experiments, unless otherwise indicated. It was essentially at the pressure antinode of the standing wave pattern.

2.2. Cavity subsystem

As shown in Fig. 1b, the axisymmetric cavity was formed by sliding a Plexiglas tube over two Plexiglas sleeves, one connected to the aluminum pipe A and the other to pipe B. Details of this general configuration are described by Rockwell et al. (2003). For all the present experiments, the cavity length and depth were maintained as $L = 63.5$ mm and $W = 12.7\,\mathrm{mm}$. In order to allow effective application of particle image velocimetry (PIV), approximately one quadrant of the Plexiglas tube was machined away and replaced by a thin plastic window. This thin window was of a 0.1 mm thick sheet of acetate, which was wrapped about the entire periphery of the interior of the Plexiglas tube, thereby forming a smooth and continuous internal surface of the cavity. The major motivation for installation of this thin plastic window was to allow recording, with insignificant refraction effects, of the particle images illuminated by the laser sheet. An additional consideration was the optimal transmission of the laser sheet through the window. The thin plastic window was designed in such a manner that it could be easily replaced when scratched or smeared with a film of oil during the seeding process for PIV. Minimization of internal reflection of the laser sheet was accomplished by spray painting the entire internal surface with flat black (nonreflecting) paint, except for the quadrant of the window employed for laser sheet transmission and recording of the particle image patterns over the field of view of the camera, which is indicated in the sectional cut at the upper right of Fig. 1b.

This special design of the thin plastic window insert, which was a thin circular cylinder, was relatively rigid in the region where it did not come into contact with the interior of the thick Plexiglas tube. In order to ensure that the possible flexibility of the window was not an issue, detailed experiments were performed and compared with the case where the thick Plexiglas tube extended about the entire periphery, as in the experiments of Rockwell et al. (2003). Both the frequencies and magnitudes of the spectral peaks of the pressure fluctuations were repeatable within two percent.

2.3. Pressure measurements

The pressure transducer a, which is located in the aluminum pipe A on the inlet side of the cavity, as indicated in Fig. 1b, served as the reference signal for the PIV measurements. It was essentially at the pressure antinode for the predominant frequency of interest. Preliminary experiments also involved acquisition of pressure data at the transducer locations b and c on the floor of the cavity and at the impingement corner. At all locations, a piezoelectric PCB pressure transducer was employed. This transducer had a nominal sensitivity of 1500 mV/psi. Adjustment of the gain of the transducer, as well as analog filtering of the transducer signal, was accomplished by use of a multi-channel signal conditioner. Gain adjustment was crucial to meet the voltage level requirements of the A/D board.

The conditioned analog pressure signals were converted to digital format by a digital, multi-channel data acquisition board, which houses one A/D converter, and can reach a sampling rate of 250 kS/s (kilosamples per second) when operating in the single mode; the effective sampling rate is reduced by a factor corresponding to the number of channels of acquired data. In order to allow the effective interpretation of the pressure signal in the time domain, i.e., to serve as a phase reference for acquisition of PIV images, a sampling rate of 20 kS/s was selected. This rate is higher than the time domain requirement of ten samples per cycle by a factor of two, but still lower than the highest possible sampling rate of the board, thereby keeping the data files relatively compact.

The experimental results of Rockwell et al. (2003) provided a basis for the selection of a locked-on flow tone. For the present cavity configuration, the inflow velocity $U = 38.22\,\mathrm{m/s}$ (130 ft/s), which corresponds to the time-averaged velocity at the centerline of the pipe, yielded a well-defined flow tone. Spectra are shown in Fig. 1c for the three locations p_a, p_b, and p_c, defined in the schematic of Fig. 1b. The dominant peak is at $f = 640\,\mathrm{Hz}$. At location p_a, which is in the pipe resonator well upstream of the cavity inlet, secondary, low-amplitude peaks correspond to the previously excited mode of the resonator at a lower value of velocity U. The dominant peak is, however, nearly one and one-half orders of magnitude larger than the secondary peak. At location p_b, which corresponds to the floor of the cavity, the background level is significantly higher, due to the enhanced, broadband turbulence of the separated flow within the cavity. Moreover, at location p_c, this background level is further enhanced due to the direct impingement of the separated shear layer upon the corner. That is, contributions from both organized vortical structures and broadband turbulence are evident in the spectrum.

The time trace of the signal at p_a within the pipe was employed as a phase reference for the image acquisition. The transducer that records p_a is nearly coincident with the location of the pressure antinode. More specifically, the distance between them is 0.039 λ_a, where λ_a is the acoustic wavelength. The spectral peak at this location has a dimensionless pressure amplitude $p/\rho_o cU = 0.0088$, which corresponds to the maximum dimensionless value of the one-dimensional acoustic particle velocity $(u_a)_o/U$. Furthermore, as shown by Rockwell et al. (2003), this locked-on state corresponds to a high value of the quality (Q) factor of the predominant spectral peak. The values of Q for pressure spectra corresponding to p_a, p_b, and p_c in Fig. 1c are respectively 568, 564 and 557. All of these values are large in comparison with the maximum attainable Q factor of the resonator pipe system in absence of throughflow, i.e., $Q \cong 80-100$, as determined from preliminary experiments. Taken together, the consistent values of Q at all transducer locations show the global nature of the locked-on flow tone. A further indication of the occurrence of the locked-on state is a large ratio of the peak pressure amplitude P to the local background pressure magnitude p_{bg} at lock-on, P/p_{bg}. For the spectrum corresponding to pressures p_a, p_b, and p_c, respective values of P/p_{bg} are 1000, 79, and 26. Clearly, the high level of broadband turbulence within the cavity substantially reduces P/p_{bg}.

This locked-on state corresponds to the coincidence of an inherent instability of the shear flow through the cavity with an acoustic resonant mode of the pipe-cavity system. It is therefore appropriate to compare the frequency of the aforementioned spectral peaks with previous correlations of the most unstable disturbance in the separated shear layer. For the present experiments, the value of the Strouhal number is $fD/U = 0.41$, which is within the band of values characteristic of a fully evolved, large-scale axisymmetric vortex formation in a free shear (jet) flow in absence of a cavity (Blake, 1986). The Strouhal number based on cavity length was $fL/U = 1.025$, which corresponds to the second shear layer mode and, thereby, occurrence of two vortical structures in the shear layer.

2.4. Techniques of high-image-density particle image velocimetry

Quantitative visualization was accomplished by a digital version of particle image velocimetry (DPIV). This approach leads to two-dimensional velocity fields over a desired cross-section of the unsteady cavity flow. In turn, other representations of the flow, such as distributions of vorticity and streamline patterns are attainable.

Effective generation of seeding particles in the airflow is central to the DPIV approach. As indicated in Fig. 1a, the relatively low speed air in the plenum chamber was seeded with olive oil particles having an effective diameter of 1 μm. Seeding was provided by a seed generator consisting of a six jet atomizer.

The laser sheet designated in Fig. 1b was generated from a dual, pulsed Nd:Yag laser system. The pulsed laser had a maximum energy output of 90 mJ, but only 20% of this available energy was used, in order to minimize internal reflections within the cavity arrangement. The output of the laser was transmitted through a spherical lens, then a cylindrical lens. The resultant laser sheet had a thickness of approximately 1 mm and a width that exceeded the cavity length. The entire arrangement of the laser and optical system was placed on a multi-degree-of-freedom positioning unit, in order to make fine adjustments of the laser sheet location, width and thickness. Such a positioning system is critical, since the acquired images are very sensitive to the alignment of the laser sheet with respect to the centerline of the cavity.

A digital charge-coupled device (CCD) camera was used to capture the pairs of single-exposed images for the cross-correlation version of DPIV. The CCD camera has a total of 1024 horizontal (H) and 1024 vertical (V) pixels, of which only 1008 (H) and 1018 (V) are light sensitive. The active imager area is of a size of 9.07 mm (H) × 9.16 mm (V), which gives a square pixel size of 9.0 μm × 9.0 μm. The camera is used at its maximum framing rate of 30 frames/s, which gives 15 sets of cross-correlated images per second. A lens of a focal length of 105 mm and an extension tube were used, thereby providing a magnification of 1:7.3.

The CCD camera and the pulsed laser were controlled by a synchronizer. The trigger signal to the lasers was also recorded with the pressure signal, in order to define the instant at which PIV images were acquired. That is, the phase of each laser pulse is designated on a given pressure signal. With this information, it was possible to determine the phase of acquisition of each image of the velocity field.

2.5. Image processing and interrogation

Software that employed a cross-correlation method involving two successive Fast Fourier transforms was used to evaluate Tagged Image File Format (TIFF) image file pairs and obtain a velocity field for each pair. An interrogation window of 16 (H) × 16 (V) pixels with a minimum of 50 particles per window ensured satisfaction of the high-image-density criterion. Due to laser light reflections immediately adjacent to the walls of the cavity, velocity vectors could not be evaluated accurately in these regions; they appear as blank strips in the images shown herein.

The post-processing of the raw velocity field involved automatic validation of the vector field by the removal of spurious vectors, replacement of the removed vectors, and implementation of a Gaussian filter with an exponent of $p = 1.3$, as discussed by Landreth and Adrian (1989). The total number of spurious vectors, however, was only two percent of the total number of vectors.

The evaluated velocity V generally includes contributions from both hydrodynamic and acoustic components. For the case addressed herein, the acoustic particle velocity u_a is, however, two orders of magnitude smaller than the mean velocity U (See Section 2.3); the evaluated velocity V is therefore essentially hydrodynamic.

2.6. Time-averaging of PIV images

Pairs of image patterns, which eventually yielded a single image of the actual velocity field, were acquired at an interval of $\frac{1}{15}$ s. If the nominal frequency of oscillation of the cavity shear layer is approximately 640 Hz, this framing rate corresponds to an interval of more than 40 cycles of oscillation. It therefore provides a suitable spacing in time for obtaining random samples for the calculation of averaged turbulence statistics. Using this approach, a total of 128 images were acquired. The definition for each of the time averages, in which N is the total number of images, is as follows:

time-averaged horizontal component of velocity,

$$\langle u \rangle \triangleq \frac{1}{N} \sum_{n=1}^{N} u_n(x, y);$$

time-averaged transverse component of velocity,

$$\langle v \rangle \triangleq \frac{1}{N} \sum_{n=1}^{N} v_n(x, y);$$

time-averaged vorticity,

$$\langle \omega \rangle \triangleq \frac{1}{N} \sum_{n=1}^{N} \omega_n(x, y);$$

root-mean-square of u component fluctuation,

$$u_{\text{rms}} \triangleq \left\{ \frac{1}{N} \sum_{n=1}^{N} [u_n(x, y) - \langle u(x, y) \rangle]^2 \right\}^{1/2};$$

root-mean-square of v component fluctuation,

$$v_{\text{rms}} \triangleq \left\{ \frac{1}{N} \sum_{n=1}^{N} [v_n(x, y) - \langle v(x, y) \rangle]^2 \right\}^{1/2};$$

averaged value of Reynolds stress correlation:

$$\langle u'v' \rangle \triangleq \frac{1}{N} \sum_{n=1}^{N} [u_n(x, y) - < u(x, y) >][v_n(x, y) - \langle v(x, y) \rangle].$$

2.7. Phase-averaging of PIV images

In addition to time-averaging, phase-averaging of images was also pursued. This approach accounts for the fact that the framing rate of the camera is much smaller than the rate of formation of vortical structures. Identification of an accurate phase reference for selection of images followed a two-step process. The first step involved a pre-classification using the sinusoidal reference pressure signal p_a within the pipe resonator as a reference. Let ϕ indicate the phase difference between the occurrence of zero pressure amplitude and acquisition of a pair of particle image patterns, i.e., a single pattern of vorticity. A total of five values of ϕ were identified over one cycle of oscillation. At each of these values of ϕ, a bandwidth of $2\Delta\phi$ was defined, in which $\Delta\phi = 36^\circ$. Only those images that fell into each of these windows of $2\Delta\phi$ at the five values of phase angle ϕ were considered in the pre-classification process. The second step, which led to accurate determination of the phase, involved the value of x_v at which a large-scale vortical structure occurred. More specifically, the centroid of vorticity of the vortical structure at x_v was determined. This second stage of the phase referencing process was necessary for two reasons. First of all, an ambiguity arises from the fact that approximately two and one-half wavelengths of the shear layer oscillation, and thereby two vortical structures, exist along the cavity. Second, the patterns of vorticity can exhibit significant jitter, even when the pointwise pressure measurements show essentially sinusoidal pressure signals and sharply defined, (high Q factor) spectra, as indicated in Section 7. It is therefore essential, if one wishes to obtain an appropriate phase average, to use this quantitative identification of x_v involving the vorticity centroid. This allowed resolution of the effective phase angle to within $\pm 1.5^\circ$.

The equations employed for phase-averaging are directly analogous to those employed for time-averaging, except the average is performed for the total number of M images at a given phase ϕ, as described in the foregoing:

phase-averaged horizontal component of velocity,

$$\langle u \rangle_p \triangleq \frac{1}{M} \sum_{m=1}^{M} u_m(x, y);$$

phase-averaged transverse component of velocity,

$$\langle v \rangle_p \triangleq \frac{1}{M} \sum_{m=1}^{M} v_m(x, y);$$

phase-averaged vorticity,

$$\langle \omega \rangle_p \triangleq \frac{1}{M} \sum_{m=1}^{M} \omega_m(x, y),$$

where M is the total number of images in a phase-average and m refers to the images selected for the phase-average. This averaging was employed for each set of phase-referenced images described in the preceding paragraph. Using this approach, it was possible to obtain a succession of phase-averaged images. For all image layouts shown herein, the nominal phase increment $\Delta\phi_p$ on the reference pressure signal is $\Delta\phi_p = 72°$.

3. Time-averaged flow structure

Time-averaged images of vorticity $\langle \boldsymbol{\omega} \rangle$, stream function $\langle \psi \rangle$ and streamwise velocity $\langle u \rangle$ are shown in Fig. 2a. At the leading-corner of the cavity, the peak vorticity has a value of $-13{,}212\,\mathrm{s}^{-1}$, and at the mid-location of the cavity, which corresponds to $x/D = 1.25$, it decreases to a significantly lower value of $-5468\,\mathrm{s}^{-1}$. This reduction in the peak value of vorticity $\langle \boldsymbol{\omega} \rangle$ in the streamwise direction involves changes of the profile of the streamwise component of velocity $\langle u \rangle$ shown in the bottom image of Fig. 2a. The vorticity thickness can be defined as $\delta_\omega = (U_1 - U_2)/[\mathrm{d}\langle u \rangle/\mathrm{d}y]_{\max}$, in which U_1 and U_2 are the free-stream velocities (or their equivalent) on the upper and lower sides of the shear layer. The vorticity thickness increases linearly along the cavity shear layer according to the relation $\delta_\omega/D = 0.143\ x/D + 0.0626$, and has a value of $\delta_\omega/D = 0.071$ near the leading-corner of the cavity at $x/D = 0.0587$ and a value of $\delta_\omega/D = 0.241$ at the mid-cavity location $x/D = 1.25$. Since the wavelength and scale of concentrations of vorticity are expected to be related to the vorticity thickness δ_ω (Monkewitz and Huerre, 1982), it follows that relatively small-scale concentrations should be present in the layer separating from the leading-corner of the cavity, while larger-scale clusters of vorticity are expected to form at locations well downstream of the leading-edge corner. In fact, this is the case, as will be addressed subsequently.

A further feature of the distributions of $\langle u \rangle$ shown in the bottom image of Fig. 2a is a relatively small magnitude of negative (reverse flow) velocity; it has a maximum value of $-[\langle u \rangle]_{\max}/U = 0.128$. This flow is necessary in order to satisfy the entrainment demands of the separated shear layer as it develops along the cavity. At the midsection of the cavity $x/D = 1.25$, the volumetric flow rate Q_r of the reverse flow, normalized by the idealized volume inflow is $-Q_r/(U\pi D^2/4) = 0.023$. This reverse flow is part of a large-scale recirculating flow pattern, which is indicated by the pattern of streamlines $\langle \psi \rangle$ in the middle image of Fig. 2a. The recirculation cell is centered close to the bottom right corner of the cavity. This pattern contrasts with the form and location of recirculation cells in deeper cavities, where one

Fig. 2. (a) Representations of time-averaged flow field. Upper image shows the averaged vorticity field, middle image gives corresponding streamline patterns viewed in a laboratory (fixed) frame and bottom image shows distributions of the streamwise component of the averaged velocity at six locations along the cavity. In the top image, the minimum contour level is $-11{,}740\,\mathrm{s}^{-1}$ and the incremental level is $1620\,\mathrm{s}^{-1}$. (b) Representations of time-averaged flow field. Upper image shows contours of constant root-mean-square of the streamwise velocity fluctuation, u_{rms}. Minimum contour level is 5.5 m/s and increment is 0.5 m/s. Middle image shows contours of constant rms of the transverse velocity fluctuation, v_{rms}. Minimum contour level is 2.84 m/s and increment is 0.57 m/s. Bottom image shows contours of constant velocity correlation, $\langle u'v' \rangle$ Minimum contour level is $-77.35\,\mathrm{m}^2/\mathrm{s}^2$ and increment is $20.1\,\mathrm{m}^2/\mathrm{s}^2$. The first level above zero is omitted for clearer illustration of the shear layer.

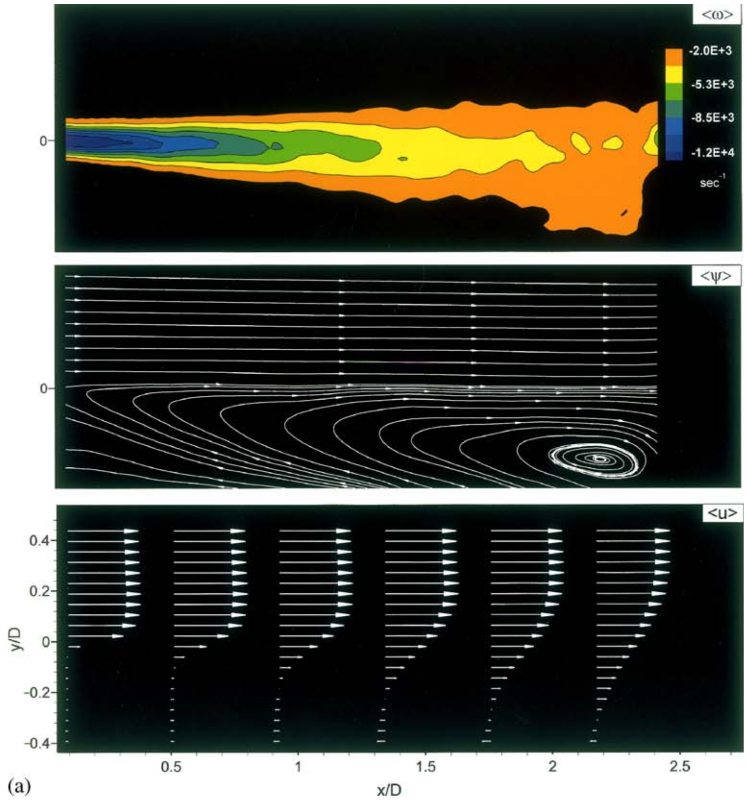
<ω>
-2.0E+3
-5.3E+3
-8.5E+3
-1.2E+4
sec^{-1}
0
<ψ>
0
<u>
0.4
0.2
0
-0.2
-0.4
y/D
0.5
1
1.5
2
2.5
x/D

(a)

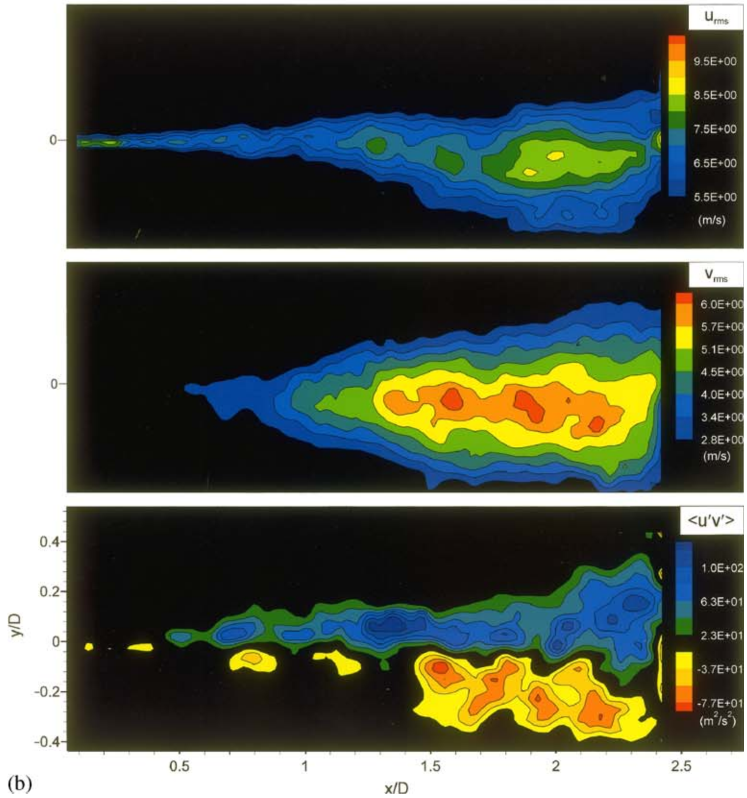
u$_{rms}$
9.5E+00
8.5E+00
7.5E+00
6.5E+00
5.5E+00
(m/s)
0
v$_{rms}$
6.0E+00
5.7E+00
5.1E+00
4.5E+00
4.0E+00
3.4E+00
2.8E+00
(m/s)
0
<u'v'>
1.0E+02
6.3E+01
2.3E+01
-3.7E+01
-7.7E+01
(m^2/s^2)
0.4
0.2
0
-0.2
-0.4
y/D
0.5
1
1.5
2
2.5
x/D

(b)

or two cells are present, and their centers are well above the cavity floor (Pereira and Sousa, 1995; Takakura et al., 1996).

Corresponding patterns of the velocity fluctuations and their correlation are given in terms of u_{rms}, v_{rms} and $\langle u'v' \rangle$ in the images of Fig. 2b. Significant values of u_{rms} occur in the shear layer immediately downstream of the leading-edge and, further downstream of this region, increasingly larger regions of higher level u_{rms} are evident. In the vicinity of the trailing-corner of the cavity, the domain of large values of u_{rms} becomes quite extensive, which suggests movement and distortion of large-scale clusters of vorticity through this region. The corresponding plot of v_{rms} shown in the middle image also indicates relatively high values of v_{rms} at locations upstream of the trailing-corner of the cavity, which again implies large-scale activity; this aspect is addressed below. The peak values of u_{rms} and v_{rms} normalized by the time-averaged inflow velocity U at the centerline of the pipe exit are $u_{\mathrm{rms}}/U = 0.233$ and $v_{\mathrm{rms}}/U = 0.163$. They occur respectively at $x/D = 2.42$ and 1.88.

The velocity correlation $\langle u'v' \rangle$, which corresponds to the predominant Reynolds shear stress component, has relatively high values along the cavity shear layer. The recirculation zone near the floor of the cavity also shows, however, a region of significant Reynolds stress of opposite sign from that in the cavity shear layer. This Reynolds stress is due to the jet-like flow along the floor of the cavity. The peak values of normalized positive and negative velocity correlation are respectively $\langle u'v' \rangle / U^2 = 0.0982$ at $x/D = 1.354$ and $y/D = 0.075$ and -0.0667 at $x/D = 1.54$ and $y/D = -0.11$. Viewing together the recirculation cell (middle image of $\langle \psi \rangle$ in Fig. 2a) and the opposite-signed layers of $\langle u'v' \rangle$ at the lower right corner of the cavity, it is evident that this region of the flow involves severe and rapid flow distortion. The averaged patterns in the images of Figs. 2a and b are intimately related to the generation of organized vortical structures in the separated shear layer along the cavity. In the next section, these features are interpreted with the aid of instantaneous and phase-averaged representations of the flow patterns.

4. Phase-averaged versus instantaneous representations of flow structure

The phase-averaging process described in Section 2.7 yields averaged images of the flow, which serve as a guide for the interpretation of instantaneous images. Fig. 3a shows patterns of phase-averaged $\langle \boldsymbol{V} \rangle_p$ and instantaneous $\boldsymbol{V}$ velocity vectors for the case where the phase-averaged vortex is close to the middle of the cavity, i.e., its center is at $x/D \cong 1.4$. The patterns of velocity vectors in all of the images are shown in a reference frame moving with 0.25 U, where U is the time-averaged velocity at the centerline of the cavity inlet; this reference frame yields swirl patterns that are centered on the extrema of vorticity. In addition to the vortex described in the foregoing, a further feature of the pattern of $\langle \boldsymbol{V} \rangle_p$ is a well-defined swirl at the right-hand side of the image. The corresponding instantaneous images indicate that this swirl has a relatively large transverse extent, in comparison with that of the phase-averaged pattern, which indicates that its instantaneous structure is not as persistent as the aforementioned vortex at the middle of the cavity.

Corresponding patterns of averaged vorticity $\langle \boldsymbol{\omega} \rangle_p$ and instantaneous vorticity $\boldsymbol{\omega}$ are shown in the images of Fig. 3b. The middle and lower images of ω were included in the calculation of the top image of $\langle \boldsymbol{\omega} \rangle_p$. Patterns of both $\langle \boldsymbol{\omega} \rangle_p$ and $\boldsymbol{\omega}$ show the tendency to form a large-scale structure, which is centered at $x/D \cong 1.4$, in accord with the centers of the swirl patterns of Fig. 3a. Further downstream, at a location immediately adjacent to the trailing-corner of the cavity, larger-scale, but considerably less coherent, clusters of vorticity are identifiable. Moreover, a prevalent feature of the instantaneous patterns of ω is the presence of small-scale vorticity concentrations in the initially separated shear layer from the leading-corner of the cavity. In fact, these small-scale concentrations are still identifiable in the larger-scale clusters of vorticity. The typical wavelength λ_{ss} between small-scale vorticity concentrations near the leading-corner of the cavity is $\lambda_{ss}/D = 0.17$. Alternately, using the vorticity thickness δ_ω defined in Section 3, $\lambda_{ss}/\delta_\omega = 2.39$. In Section 5, these values of wavelength will be compared with the dimensionless wavelength λ between the large-scale vortical structures, which scale on diameter D, since they are related to a fully evolved axisymmetric instability of the jet (Rockwell et al., 2003).

Inspection of a large number of instantaneous images shows that the small-scale vortical structures tend to form around the periphery of the large-scale vorticity cluster. That is, the layer of small-scale concentrations rolls up to form the large-scale cluster of vorticity. The small-scale concentrations are, however, not phase-locked to the generation of the large-scale vortex. Neither their generation from the leading-corner of the cavity nor their rollup into the large-scale vortex is accounted for in the phase referencing criteria described in Section 2.7, which focuses on the large-scale vortex. This non-phase-locked development of the patterns of small-scale vorticity is, in turn, related to jitter of the position and form of the large-scale vortex formation. It blurs the phase-averaged representation $\langle \omega \rangle_p$ of the large-scale vortex, which is shown in the pattern of phase-averaged vorticity $\langle \omega \rangle_p$ in the top image. The highest values of vorticity are near the center of the cluster of large-scale vorticity.

Viewing the patterns of vorticity in Fig. 3b as a whole, it is evident that large-scale vortical structures form in a well-defined separated shear layer along the relatively shallow cavity. Referring to Fig. 2a, the inflection point of the profile of the streamwise velocity component $\langle u \rangle$ remains a significant distance above the floor of the cavity over its entire length. One expects, however, that if the cavity were to be sufficiently shallow, i.e., the depth W/D would become sufficiently small, the distributions of $\langle u \rangle$ shown in the bottom image of Fig. 2a would be distorted, and the development of large-scale vortices may be attenuated. The drastic decrease in amplitude of the pressure fluctuations at smaller W/D, characterized by Rockwell et al. (2003), suggests that vortex formation is inhibited.

It is insightful to evaluate the values of dimensionless circulation $\Gamma^* = \Gamma/\pi UD$ for both the small- and large-scale concentrations of vorticity shown in the instantaneous images of Fig. 3b. For the small-scale concentrations, which occur immediately downstream of the leading-corner of the cavity, the values of Γ^* are approximately in the range of $0.004 \lesssim \Gamma^* \lesssim 0.01$. Regarding the large-scale cluster of vorticity, which is particularly well defined in the bottom image and approximately centered at $x/D \cong 1.4$, the value of $\Gamma^* \cong 0.26$. It is therefore evident that the value of Γ^* of a typical large-scale vortical structure exceeds that of the initially formed small-scale vortex by more than an order of magnitude.

It is insightful to compare, in each image of Fig. 3b, the value of Γ^*_{vortex} of the well-defined large-scale vortex at the center of each image (referred to in the foregoing paragraph), with the value of $\Gamma^*_{\text{pre-vortex}}$, which represents the integrated vorticity in the layer prior to vortex formation, and includes both the aforementioned small-scale vorticity

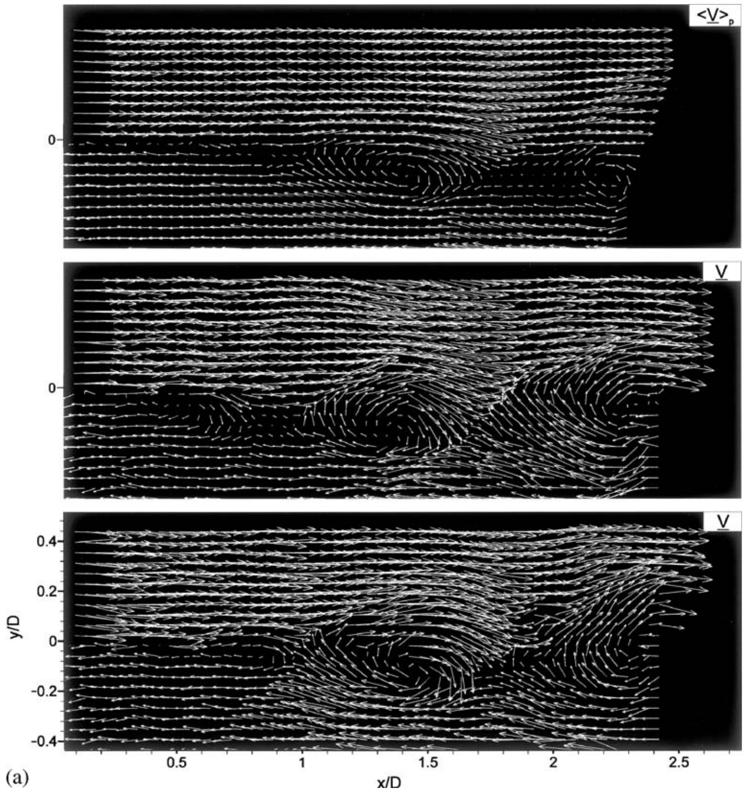

Fig. 3. (a) Comparison of the phase-averaged pattern of velocity vectors (top image) with two patterns of instantaneous velocity vectors (middle and bottom images). Both the middle and bottom images were included in the phase-averaging process that yielded the top image. All three images are in a reference frame moving at 0.25 U, where U is the time-averaged velocity at the centerline of the cavity inlet. (b) Comparison of the phase-averaged pattern of vorticity (top image) with instantaneous patterns of vorticity (middle and bottom images). Both the middle and bottom images were included in the phase-averaging process that yielded the top image. In all three images, the minimum contour level is $-16{,}000\,\text{s}^{-1}$ and the increment is $1280\,\text{s}^{-1}$. The first level above zero, as well as below zero, is omitted for clearer illustration of the flow structure. (c) Comparison of phase-averaged pattern of transverse velocity (top image) with instantaneous patterns of transverse velocity (middle and bottom images). Both the middle and bottom images were included in the phase-averaging process that yielded the top image. In the top image, the minimum contour level is -5.63 m/s and the increment is 0.81 m/s. In the middle and bottom images, the minimum contour level is -12.06 m/s and the increment is 1.47 m/s. In both instantaneous images, the first level above zero is omitted for clearer illustration of the flow structure.

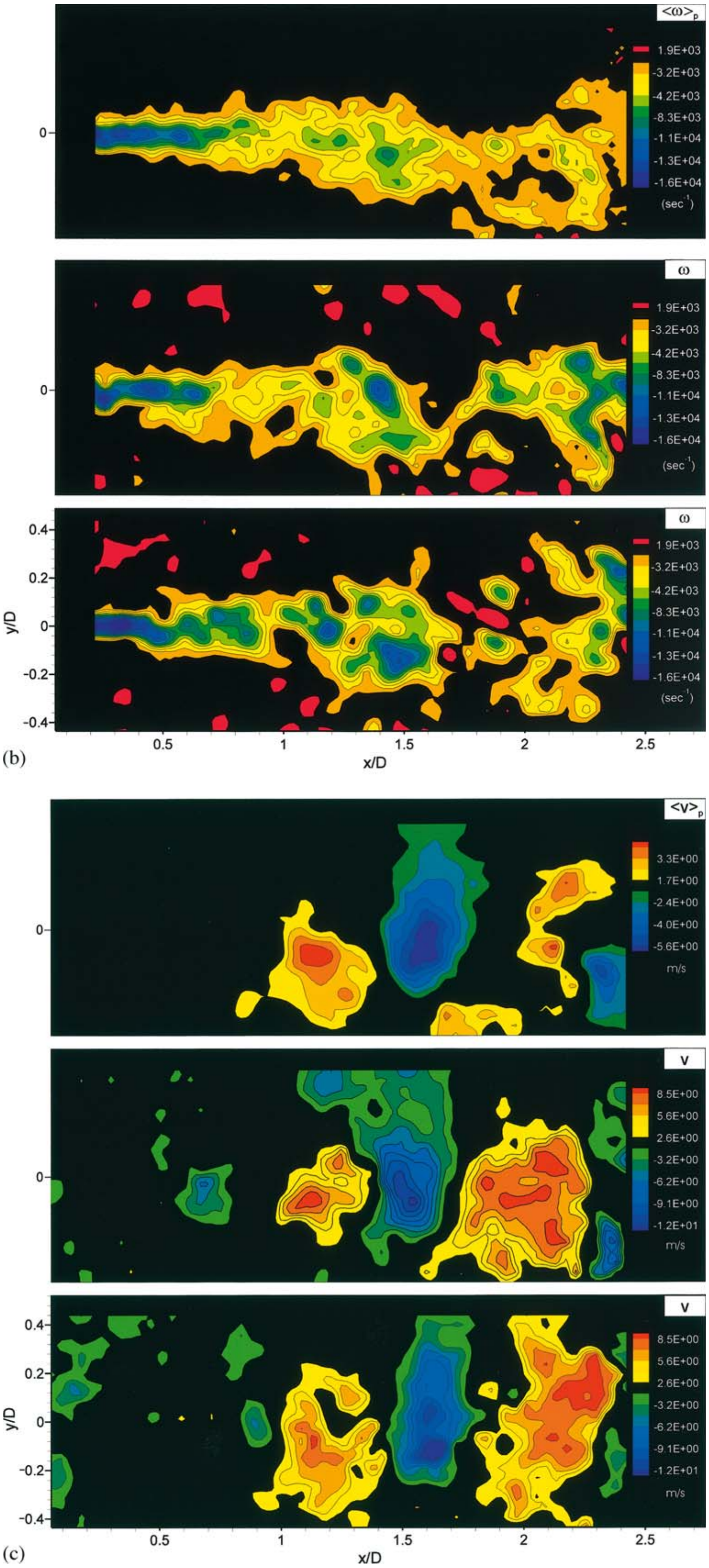

Fig. 3 (*continued*).

Table 1
Comparison of values of dimensionless circulation Γ^* for various regions of the cavity shear layer

	Γ^*_{vortex}	$\Gamma^*_{\text{pre-vortex}}$	Γ^*_{total}
Top image	0.23	0.24	0.66
Middle image	0.22	0.25	0.70
Bottom image	0.29	0.23	0.75

concentrations and the distributed (nonconcentrated) vorticity. The domain of the vorticity field of the shear layer included for calculation of $\Gamma^*_{\text{pre-vortex}}$ extends from the pipe exit to the streamwise location at which the first large-scale concentration of vorticity begins.

The circulation Γ^*_{total} accounts for all of the vorticity in the image. In this evaluation, the locations of the left and right-boundaries of a given large-scale vortex correspond to the pinched sections (minimum cross-sectional areas) of the vorticity contours. Table 1 provides a comparison of the values of Γ^* for each image of Fig. 3. The values of Γ^* are remarkably close for all of these images, which includes both phase-averaged and instantaneous representations. Furthermore, the circulation of the layer $\Gamma^*_{\text{pre-vortex}}$ prior to vortex formation is approximately equal to the vortex circulation Γ^*_{vortex}.

An indication of the magnitude of the undulations of the shear layer along the cavity is provided by the variation of the transverse (vertical) velocity component v. Fig. 3c gives contours of constant phase-averaged (transverse) velocity $\langle v \rangle_p$ in the top image, as well as instantaneous (transverse) velocity v in the middle and bottom images. In all images, it is evident that a substantial transverse (vertical) gradient of the phase-averaged $\langle v \rangle_p$ and instantaneous v velocity occurs at a given value of streamwise distance x/D. The spatially nonhomogeneous development of the shear layer along the cavity, its impingement upon the trailing-corner, and the proximity of the floor of the cavity to the shear layer, are all associated with the lack of spatial periodicity of the patterns of phase-averaged velocity $\langle v \rangle_p$ and instantaneous velocity v. Nevertheless, it is possible to obtain an estimate of the streamwise wavelength λ/D, which is the distance between either positive or negative extrema of $\langle v \rangle_p$. For the phase-averaged representation shown in the top image of Fig. 3c, the value of dimensionless wavelength is approximately $\lambda/D \cong 1.0$, while for the instantaneous patterns in the middle and bottom images, the corresponding values lie in the range $0.90 \lesssim \lambda/D \lesssim 0.95$. These patterns of Fig. 3c show the difficulty of attempting to deduce values of λ/D on the basis of a constant elevation y/D, which is the traditional approach employed for pointwise measurements of this class of flows, as assessed by Rockwell (1983).

5. Space–time evolution of flow patterns

In order to show the variation of spatial representations of velocity, vorticity and streamline topology at successive phases of the oscillation cycle, phase-averaged representations of the images were employed. An overview of the basic types of images is given in Fig. 4. The top image shows phase-averaged velocity vectors $\langle V \rangle_p$ in a frame of reference moving at 0.25 U. This frame results in a location of the center of the swirl pattern that is nearly coincident with the location of maximum vorticity in the corresponding image of phase-averaged vorticity $\langle \omega \rangle_p$, which is given in the middle image. The pattern of phase-averaged streamlines $\langle \psi \rangle_p$, which is shown in the bottom image of Fig. 4, is determined from the pattern of velocity vectors in the laboratory reference frame. The focus of the swirling streamline pattern is at essentially the same value of x/D as for the aforementioned maximum vorticity $\langle \omega \rangle_p$ and center of the swirl pattern of velocity vectors $\langle V \rangle_p$, which are shown respectively in the middle and top images. The vertical location of the focus of the streamline is, however, substantially lower than the centers of the patterns in the top two images. Patterns of velocity vectors and streamlines in a moving reference frame are usually indicative of the locations of the centers of large-scale vortical structures shown in patterns of vorticity, provided the proper frame velocity is selected. This general agreement is evident in the top two images of Fig. 4. On the other hand, patterns of either streamlines or velocity vectors in the laboratory reference frame may not bear a one-to-one correspondence to the actual centers of large-scale clusters of vorticity. In fact, the location of a focus, i.e., an apparent center of a spiraling streamline, can be substantially displaced from the actual location of the center of a large-scale vorticity concentration. Such is the case for a spiral pattern at the lower right of Fig. 4.

The evolution of patterns of phase-averaged vorticity $\langle \omega \rangle_p$ and velocity $\langle V \rangle_p$ is shown for three successive phases of the oscillation cycle in Fig. 5a. The large-scale swirl patterns indicated by the velocity vectors beneath each respective vorticity image are generally aligned with the regions of maximum vorticity and, moreover, the transverse (vertical)

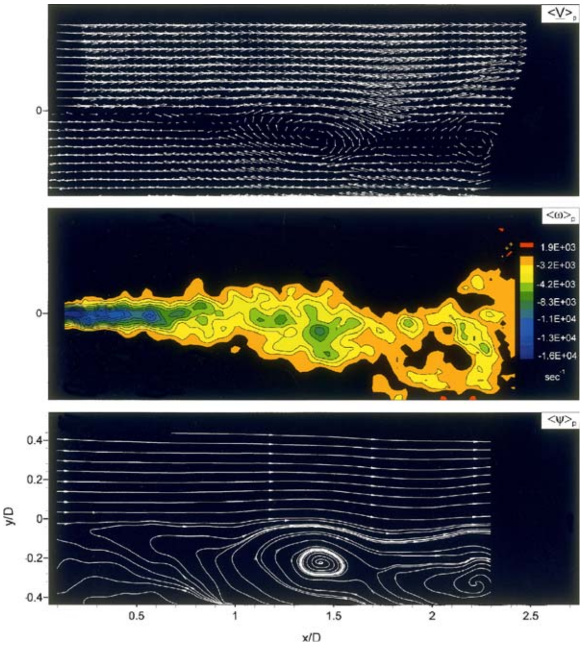

Fig. 4. Representations of the phase-averaged flow field. Top image shows phase-averaged velocity in a frame moving at 0.25 U, where U is the time-averaged centerline velocity at the cavity inlet. The middle image illustrates the phase-averaged vorticity, and the bottom image gives the phase-averaged streamlines in the laboratory (fixed) frame. In the middle image, the minimum contour level is $-16{,}000\,\mathrm{s}^{-1}$ and the increment is $1280\,\mathrm{s}^{-1}$. The first two levels above and below zero are omitted for clearer demonstration of the flow structure.

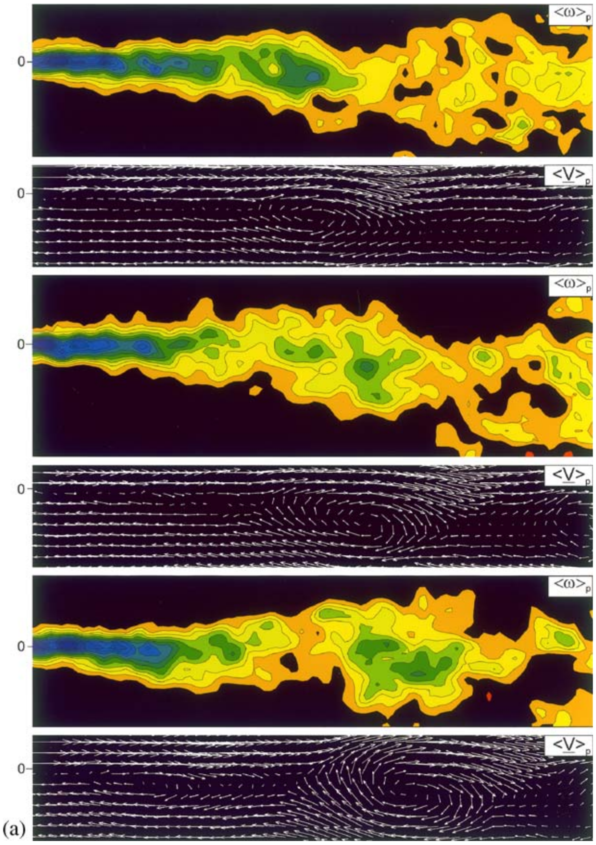

extent of these swirl patterns is in accord with the increase in size of the large-scale clusters of vorticity. The large-scale cluster continuously develops to the point where, in the bottom image of vorticity $\langle\omega\rangle_p$, it appears as a distinct entity. The agglomeration of vorticity in successive images to yield the distinct cluster shown in the bottom image does not, however, involve a significant change in the value of dimensionless circulation $\Gamma^* = \Gamma/\pi UD$, provided that the value of Γ is determined as follows. In each image, the circulation Γ was calculated from the area integral of vorticity. The domain of calculation extended a distance of 0.42 D in either direction from the location of maximum vorticity, which corresponded to the distance to the edges of the large-scale cluster of vorticity in the bottom image. Using this approach, the values of dimensionless circulation fall in the range of $0.19 \lesssim \Gamma^* \lesssim 0.21$ for all images, which indicates that the redistribution of vorticity into a large-scale cluster occurs in absence of significant diffusion effects. The consequence of this redistribution on the generation of acoustic power will be addressed below.

Values of circulation Γ^*_{vortex} of the well-defined large-scale vortex, $\Gamma^*_{\text{pre-vortex}}$, which corresponds to the vorticity in the layer prior to separation, and Γ^*_{total}, which accounts for the vorticity exhibited in the image, can be determined in the same manner as for Fig. 3b (see Table 1) and are given in Table 2.

The value of Γ^*_{vortex} increases significantly from the top to the middle image, due to the increased agglomeration of vorticity during formation of the large-scale vortex. For all images, the value of $\Gamma^*_{\text{pre-vortex}}$ is of the same order as Γ^*_{vortex}, which is similar to the finding of Table 1. This observation suggests that the vorticity in the shear layer located upstream of the large-scale vortex will play a significant role in the generation of acoustic power, as will be addressed in Section 6.

It is interesting to note that the value of Γ^* of large-scale Kármán vortex formation from a cylinder of diameter D in a freestream of velocity U is of the order of unity, i.e., $\Gamma^* \cong 1$, as measured by Green and Gerrard (1993). A further feature that can be deduced from the bottom vorticity image of Fig. 5a is the streamwise length scale ℓ of the distinct, large-scale cluster of vorticity, which is the streamwise distance between the edges of the lowest closed vorticity contour. It has a value of $\ell/D = 0.84$. This value is substantially larger than the corresponding streamwise length scale ℓ_{ss} of the small-scale concentrations of vorticity shown in the patterns of instantaneous vorticity of Fig. 3b. On the basis of those patterns, $0.1 \lesssim \ell_{ss}/D \lesssim 0.15$.

Patterns of corresponding streamlines in the laboratory frame of reference are shown in Fig. 5b. The effect of the large-scale clusters of vorticity of Fig. 5a is to induce foci (centers) of the spiraling streamline patterns that are significantly below the regions of maximum vorticity in each of the respective images. The streamline patterns, which are centered at the same streamwise location as the large-scale clusters of vorticity, undergo changes with successive phases of the oscillation cycle, i.e., in the top, middle and bottom images of Fig. 5b. In the top image, the pattern shows an outward spiral of streamlines with no limit cycle, i.e., no closed streamline. At a later phase, corresponding to the middle image, the innermost streamline pattern spirals outward to a limit cycle; exterior to this limit cycle, the pattern spirals inward, corresponding to a stable limit cycle. Finally, in the bottom image, where the cluster of vorticity of Fig. 5a is particularly large, the size of the limit cycle has become quite large; inside it, the streamline spirals inward, while exterior to it, the spiral is in the outward direction, which corresponds to an unstable limit cycle. Moreover, for this phase of the shear layer development, a second limit cycle is evident at a location further upstream.

Viewing together all of the streamline patterns of Fig. 5b, the centers of all of these spirals are at vertical locations between the locus of maximum vorticity along the shear layer (compare top image of Fig. 2a) and the floor of the cavity, which is located at $y/D = -0.5$. The spirals do not, however, have a relationship to the stationary "cells" that typically exist within a cavity. They do contribute, however, to the time-averaged topology of the streamlines, which is shown in Fig. 2a. This streamline pattern shows a single, steady recirculation eddy, or cell, that is located at the lower right-hand corner of the cavity. In other words, the streamline patterns of Fig. 5b are simply linked to the occurrence of definable, large-scale clusters of vorticity in the shear layer, and they are centered below the vorticity concentrations due to the reference (laboratory) frame of observation.

The evolution of patterns of phase-averaged vertical velocity $\langle v\rangle_p$, which correspond to the patterns of vorticity, velocity and streamline topology shown in Figs. 5a and b, is given in Fig. 5c. The middle pattern of Fig. 5a is the same as the top pattern of Fig. 3b. The succession of images of Fig. 5c, from top to bottom, corresponds to increasing scale of the large-scale cluster of vorticity. Correspondingly, the spatial extent of regions of high positive and negative v increases from the top to bottom images of Fig. 5c. In the top image, it is not possible to identify a characteristic

◀

Fig. 5. (a) Phase-averaged patterns of vorticity and velocity at successive phases of the oscillation cycle. For the vorticity patterns, the minimum contour level is $-16{,}000\,\mathrm{s}^{-1}$ and the increment is $1280\,\mathrm{s}^{-1}$. The first two levels above and below zero are omitted for clearer illustration of the flow structure. Color-coding for vorticity levels is the same as for Fig. 4. (b) Phase-averaged streamlines in the laboratory (fixed) reference frame at successive phases of the oscillation cycle. (c) Contours of phase-averaged transverse velocity at successive phases of the oscillation cycle. In all three images, the minimum contour level is -5.63 m/s and the increment is 0.81 m/s. The first two levels above and below zero are omitted for clearer illustration of the flow structure.

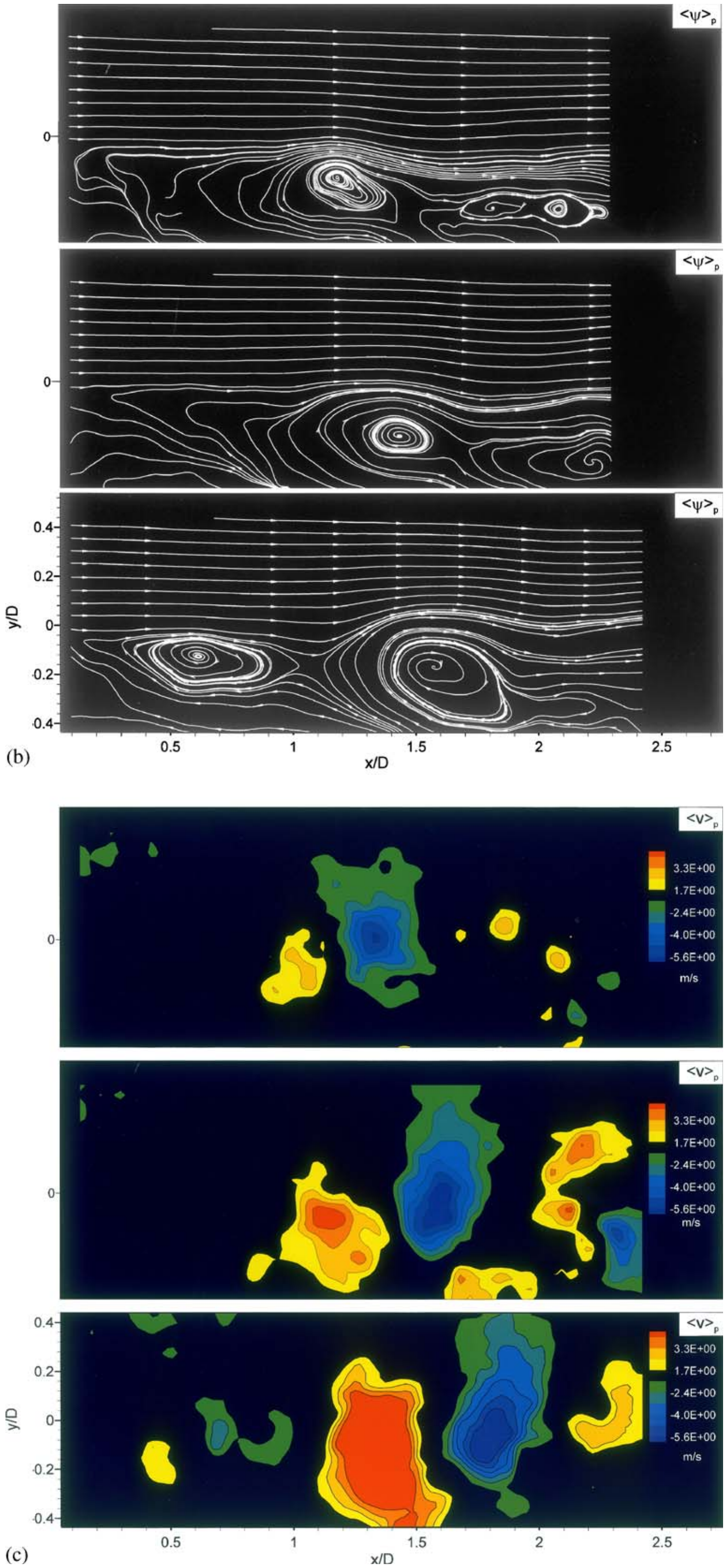

Fig. 5 (*continued*).

Table 2
Comparison of values of dimensionless circulation Γ^* for various regions of the cavity shear layer

	Γ^*_{vortex}	$\Gamma^*_{\text{pre-vortex}}$	Γ^*_{total}
Top image	0.18	0.23	0.65
Middle image	0.23	0.24	0.66
Bottom image	0.26	0.31	0.66

wavelength λ. In the middle and bottom images, the streamwise wavelengths between centers of the highest values of positive $\langle v \rangle_p$ are $\lambda/D = 1.02$ and 0.97, respectively. These values compare well with those deduced from the phase-averaged and instantaneous images of Fig. 3b, which indicates that the value of λ/D remains relatively constant as the vortex pattern evolves over the streamwise distance indicated in Fig. 5c. Using the types of images shown in Fig. 5c, it is also possible to determine the dimensionless phase speed c_v/U. If a total of five phases are considered, the average value is $c_v/U = 0.48$, with a deviation of less than six percent. The phase speed c_v/U was determined by evaluating the average streamwise velocity of a large-scale cluster of vorticity over the streamwise distance extending from $x/D = 1.21$ to $x/D = 1.60$. The foregoing information on wavelength λ/D and phase speed c_v/U can provide a quantitative basis for interpretation of the well-known correlations of the form $fL/U = (c_v/U)(n + a)$, in which n is the stage or mode number. In essence, it represents the number of wavelengths of the undulating shear layer along the cavity. Symbol a is an end correction. Various models, which employ different values of dimensionless phase speed c_v/U and end correction a are described by Rockwell et al. (2003). The aforementioned images show an averaged value of wavelength $\lambda/D \cong 1$ for the undulating shear layer, in comparison with the cavity length $L/D = 2.5$. Therefore, $n = 2$ and $a = 0.5$. Using these values, along with the experimentally determined phase speed $c_v/U = 0.48$, $fL/U = 1.2$. This value compares with the value determined from the raw values of $f = 640\,\text{Hz}$ and $U = 38.22\,\text{m/s}$, i.e., $fL/U = 1.0$. The difference between these values is most likely due to the spatial nonhomogeneity of the initial region of development of the separated shear layer downstream of the leading-corner of the cavity. In this region, the values of c_v/U and λ/D are expected to vary with streamwise distance x, in contrast to regions further downstream, where they appear to be relatively constant, as indicated in the foregoing evaluation of the images.

6. Relation of flow patterns to acoustic power integral

The vorticity field along the cavity is related to the generation of acoustic power according to the relationship established by Howe (1975, 1980):

$$\langle P \rangle = -\rho_0 \int \langle (\boldsymbol{\omega} \times \boldsymbol{V}) \cdot \boldsymbol{u}_a \rangle \, \mathrm{d}\forall, \tag{1}$$

in which ρ_0 is the density, $d\forall$ is the elemental volume, $\boldsymbol{\omega}(x,y)$ and $\boldsymbol{V}(x,y)$ are the vorticity and velocity of the hydrodynamic field and $\boldsymbol{u}_a$ is the acoustic particle velocity. The integrand of Eq. (1) can be decomposed into projections in the streamwise x and transverse y directions as follows:

$$\{[\langle \boldsymbol{\omega} \rangle_p \times \langle \boldsymbol{V} \rangle_p]_x \boldsymbol{i} + [\langle \boldsymbol{\omega} \rangle_p \times \langle \boldsymbol{V} \rangle_p]_y \boldsymbol{j}\} \cdot \{[\boldsymbol{u}_a]_x \boldsymbol{i} + [\boldsymbol{u}_a]_y \boldsymbol{j}\}, \tag{2}$$

where $\boldsymbol{i}$ and $\boldsymbol{j}$ are the unit vectors in the x and y directions. The emphasis here is, first of all, on determination of the vectors $\boldsymbol{\omega} \times \boldsymbol{V}$, then the x and y projections of this vector field according to $[\boldsymbol{\omega} \times \boldsymbol{V}]_x$ and $[\boldsymbol{\omega} \times \boldsymbol{V}]_y$. It should be emphasized that, for our present considerations, the vorticity $\boldsymbol{\omega}$ and velocity $\boldsymbol{V}$ will not be decomposed into time-averaged and fluctuating contributions. The consequence of this decomposition on the term $\boldsymbol{\omega} \times \boldsymbol{V}$ and its projections in the x and y directions is beyond the scope of this work.

Fig. 6a shows vectors of $\langle \boldsymbol{\omega} \rangle_p \times \langle \boldsymbol{V} \rangle_p$ for three successive phases of the oscillation cycle. For purposes of comparison, the corresponding patterns of phase-averaged vorticity $\langle \boldsymbol{\omega} \rangle_p$ are illustrated immediately beneath each image. All images of $\langle \boldsymbol{\omega} \rangle_p \times \langle \boldsymbol{V} \rangle_p$ show relatively large vertical, downward-oriented vectors, which are primarily due to the high values of $\boldsymbol{\omega}$ immediately downstream of the leading-corner of the cavity. With increasing streamwise distance, the magnitudes of these vectors decrease somewhat until, at the location of the large-scale cluster of vorticity, significant vertical and horizontal vectors of opposing signs are clearly evident, especially for the largest-scale cluster of vorticity shown at the bottom of Fig. 6a.

Fig. 6b shows the transverse projections of the hydrodynamic contribution to the acoustic power integral for the phase-averaged patterns in Fig. 6a. As shown in Fig. 6a, the agglomeration of vorticity leads to a more clearly defined, distinct cluster of vorticity at larger streamwise distances. This agglomeration results in regions of larger spatial extent of high levels of $[\langle \boldsymbol{\omega} \rangle_p \times \langle \boldsymbol{V} \rangle_p]_y$. Irrespective of the level of $[\langle \boldsymbol{\omega} \rangle_p \times \langle \boldsymbol{V} \rangle_p]_y$, however, it has the same sign throughout the shear layer. Correspondingly, the sequence of images of Fig. 6c shows the streamwise projections of the hydrodynamic contribution $[\langle \boldsymbol{\omega} \rangle_p \times \langle \boldsymbol{V} \rangle_p]_x$. In this series, the effect of the increased agglomeration of vorticity is

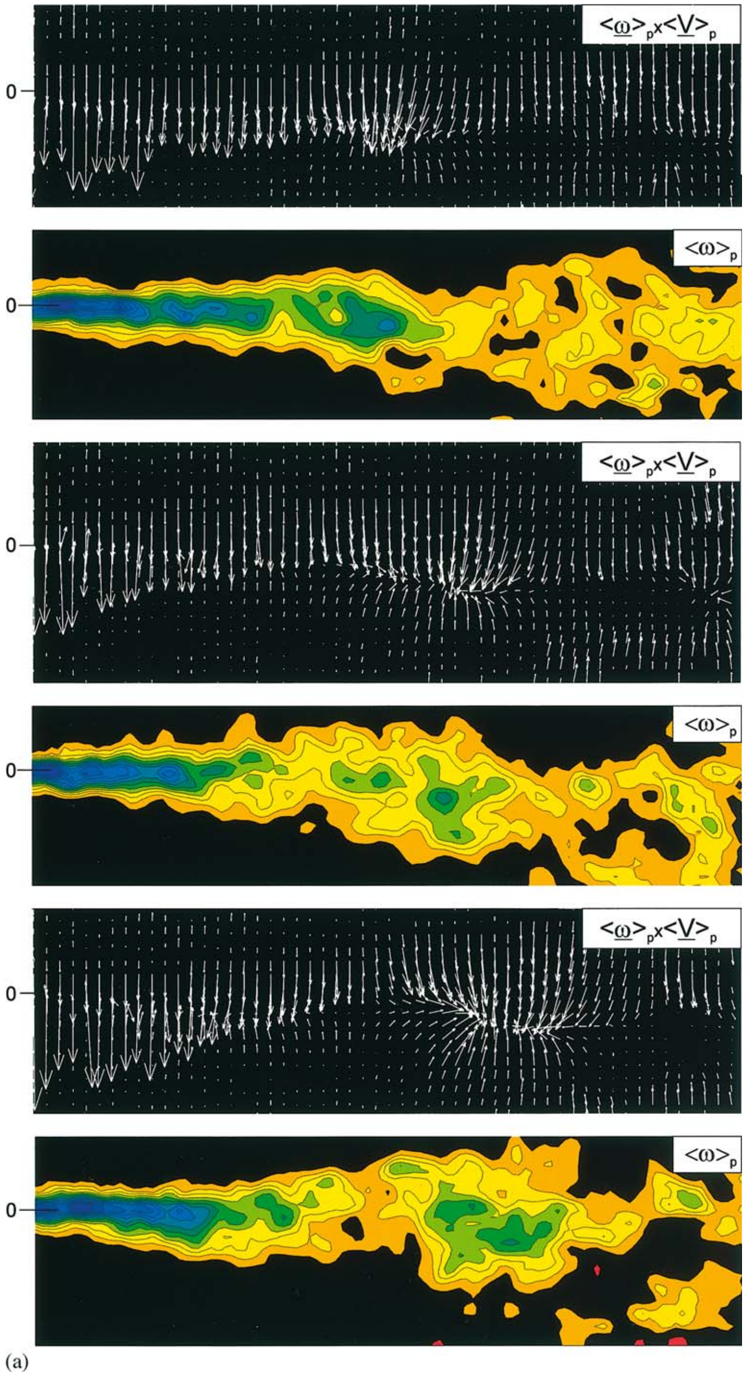

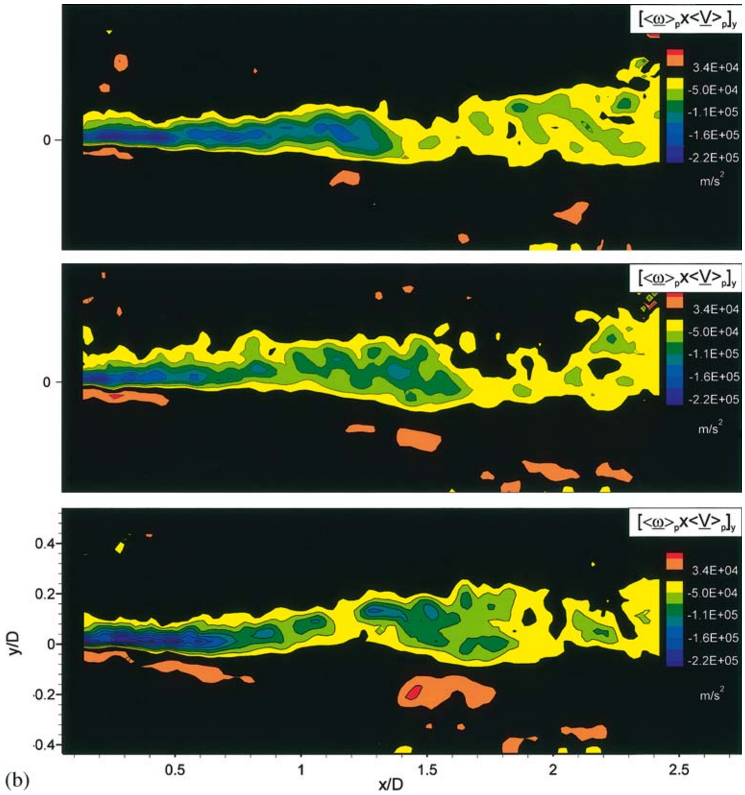

Fig. 6 (*continued*).

even more evident, as the spatial extent of large values of $[\langle \boldsymbol{\omega} \rangle_p \times \langle \boldsymbol{V} \rangle_p]_x$ increases at larger values of streamwise distance along the cavity. Moreover, adjacent clusters of $[\langle \boldsymbol{\omega} \rangle_p \times \langle \boldsymbol{V} \rangle_p]_x$ can have opposite signs.

Fig. 6d shows the transverse projections of the hydrodynamic contributions to the acoustic power integral for the same phase of the oscillation cycle as the middle set of images of Fig. 6a. Both phase-averaged $[\langle \boldsymbol{\omega} \rangle_p \times \langle \boldsymbol{V} \rangle_p]_y$ and instantaneous $[\boldsymbol{\omega} \times \boldsymbol{V}]_y$ are depicted. The top image of Fig. 6d, which is the phase-averaged representation $[\langle \boldsymbol{\omega} \rangle_p \times \langle \boldsymbol{V} \rangle_p]_y$, shows that the highest levels are indeed at locations immediately downstream of the leading-corner of the cavity, as evident in the corresponding vector plot of Fig. 6a. Significant levels persist up to about $x/D = 1.6$. At locations further downstream, generally lower levels are apparent. The corresponding images of instantaneous $[\boldsymbol{\omega} \times \boldsymbol{V}]_y$ shows high levels of $[\boldsymbol{\omega} \times \boldsymbol{V}]_y$ immediately downstream of the leading-corner of the cavity and, in addition, a number of

Fig. 6. (a) Representations of the hydrodynamic contribution to the acoustic power integral at three successive phases of the oscillation cycle. Corresponding patterns of phase-averaged vorticity are shown for purposes of comparison. (b) Transverse (y direction) projections of the magnitude of the hydrodynamic contribution to the acoustic power integral corresponding to the evolution of the phase-averaged patterns of Fig. 6a. Images show constant contours of this quantity. In all images, the minimum contour level is $-218{,}092\,\mathrm{m/s^2}$ and the increment is $28{,}064\,\mathrm{m/s^2}$. The first level above zero is omitted for clearer illustration of the shear layer. (c) Streamwise (x direction) projections of the magnitude of the hydrodynamic contribution to the acoustic power integral corresponding to the evolution of the phase-averaged patterns of Fig. 6a. Images show constant contours of this quantity. In all images, the minimum contour level is $-33{,}545\,\mathrm{m/s^2}$ and the increment is $5895\,\mathrm{m/s^2}$. The first level above zero is omitted for clearer illustration of the shear layer. (d) Transverse (y direction) projections of the magnitude of the hydrodynamic contribution to the acoustic power integral. Images show constant contours of this quantity. Upper image represents the phase-averaged pattern. The middle and bottom images show instantaneous patterns. The minimum contour level is $-215{,}540\,\mathrm{m/s^2}$ and the increment is $30{,}616\,\mathrm{m/s^2}$. (e) Streamwise (x direction) projections of the magnitude of the hydrodynamic contribution to the acoustic power integral. Images show constant contours of this quantity. Upper image represents the phase-averaged pattern. The minimum contour level is $-33{,}544\,\mathrm{m/s^2}$ and the increment is $5896\,\mathrm{m/s^2}$. The middle and bottom images show instantaneous patterns. The minimum contour level is $-101{,}320\,\mathrm{m/s^2}$ and the increment is $11{,}988\,\mathrm{m/s^2}$.

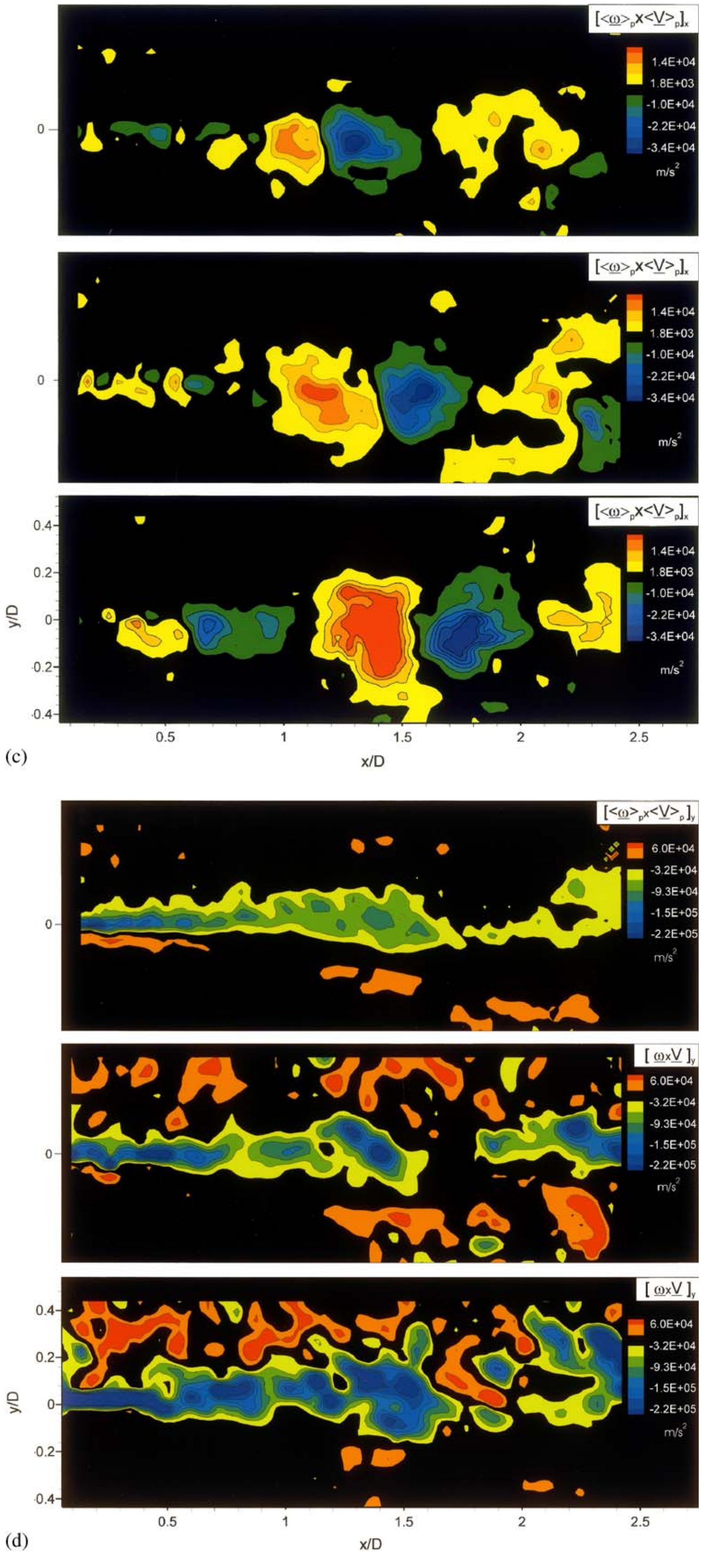

Fig. 6 (*continued*).

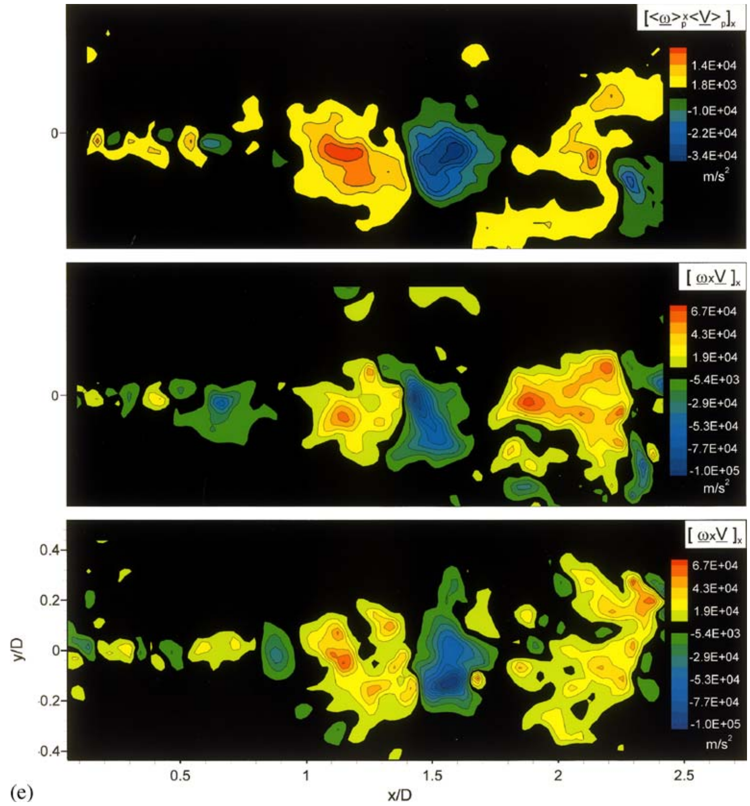

Fig. 6 (*continued*).

concentrated regions at locations further downstream. They are due to the instantaneous, small-scale vorticity concentrations shown in the instantaneous images of Fig. 3b.

Patterns of phase-averaged $[\langle \boldsymbol{\omega} \rangle_p \times \langle \boldsymbol{V} \rangle_p]_x$ and instantaneous $[\boldsymbol{\omega} \times \boldsymbol{V}]_x$, which represent projections in the streamwise (x) direction, are given in Fig. 6e. All images show that the highest positive and negative levels are associated with the large-scale cluster of vorticity (compare Fig. 3b). That is, the largest negative values tend to occur in the phase-averaged representation (top image) at $x/D = 1.55$ and the largest positive contributions at $x/D = 1.18$. The corresponding location of the large-scale, phase-averaged vorticity is at $x/D = 1.4$ (compare Fig. 3b). The overall form and general locations of the maximum positive and negative values in the instantaneous images of Fig. 6e are generally similar.

Comparison of the peak values of the phase-averaged representations of the transverse (y) and streamwise (x) contributions, which are given in Figs. 6d and e, provides the following observations. The peak value of the transverse projection $[\langle \boldsymbol{\omega} \rangle_p \times \langle \boldsymbol{V} \rangle_p]_y$, which occurs near the leading-corner of the cavity, is $-246{,}152\,\mathrm{m/s^2}$; this value is located within the minimum contour level of the top image of Fig. 6d. In comparison, the peak values of the streamwise projection $[\langle \boldsymbol{\omega} \rangle_p \times \langle \boldsymbol{V} \rangle_p]_x$ are of the order of $-40{,}000\,\mathrm{m/s^2}$, within the minimum contour level, in the top image of Fig. 6e. These peak values occur at the location where a large-scale cluster of vorticity appears near the mid-region of the cavity. It is evident from Eq. (1) that the dot product between the hydrodynamic contribution and the acoustic particle velocity, i.e., $(\boldsymbol{\omega} \times \boldsymbol{V}) \cdot \boldsymbol{u}_a$, determines the effectiveness of the acoustic power generation. For the phase of the oscillation cycle represented in Fig. 6d and e, one arrives at the following observations. The direction of the acoustic particle velocity $\boldsymbol{u}_a$ is, within the inlet and outlet pipes, in the streamwise (x) direction. Near the leading- and trailing-edges of the cavity, however, a significant component in the y direction is expected to be present, i.e., $[u_a]_y$ in Eq. (2) will be nonzero. It is therefore expected that the relatively high values of the phase-averaged projection of the transverse component of the hydrodynamic contribution $[\langle \boldsymbol{\omega} \rangle_p \times \langle \boldsymbol{V} \rangle_p]_y$, which occurs at a relatively high level near the leading-corner of the cavity could, in conjunction with the significant value of $[\boldsymbol{u}_a]_y$ in that region, produce a significant contribution to the acoustic power integral. Similarly, detectable contributions may be apparent near the trailing-corner of the cavity, where much lower level, but nevertheless discernible, values of $[\langle \boldsymbol{\omega} \rangle_p \times \langle \boldsymbol{V} \rangle_p]_y$ occur. Over the central region of the cavity, where the streamwise projection $[\boldsymbol{u}_a]_x$ is expected to dominate the magnitude of the acoustic particle velocity, contributions from the large-scale cluster of vorticity are expected to be significant, which is evident from relatively high levels in the top image of Fig. 6e. Note, however, that regions of both positive and negative $[\langle \boldsymbol{\omega} \rangle_p \times \langle \boldsymbol{V} \rangle_p]_x$ occur adjacent to each other, and their effect will tend to cancel.

7. Flow patterns due to deviations from locked-on states

The primary emphasis of the present work is on the locked-on states of large-scale vortex development in the separated shear layer. As indicated in Section 2.7, two criteria were employed in order to assess the phase-locked flow patterns: (a) all selected images must occur within the same band of narrowly defined phase on the reference pressure signal; and (b) the centers of the vorticity concentrations of the large-scale structures must occur at a given value of streamwise distance along the cavity. Examination of the entire sequence of images showed, however, that even though condition (a) was satisfied, condition (b) was not necessarily satisfied by all images.

Fig. 7a shows representative instantaneous images. The top image is from the phase-locked sequence; it satisfies criteria (a) and (b). The middle and bottom images correspond to the left and right sidebands of the locked-on state. That is, they correspond to images that satisfy condition (a) but not (b). The middle image shows a large-scale concentration of vorticity that occurs to the left of the center of vorticity of the top image, whereas the bottom image shows a concentration located to the right of the center of the top image. All of the patterns of Fig. 7a occur when the reference pressure signal is essentially sinusoidal, which is indicative of a locked-on resonator response. This suggests that effective and consistent excitation of an acoustic resonator can occur in the presence of intermittency between locked-on and nonlocked-on states of the flow patterns. Apparently, the fact that the resonator is lightly damped means that it requires a large number of oscillation cycles to decay from a given state of excitation, thereby allowing a degree of intermittency in the locked-on patterns of vortex formation. The present situation contrasts with previous investigations, involving pointwise measurements, which show intermittency of a detected velocity or pressure signal due to departures from a locked-on state, arising from the fact that a threshold sound level has not been achieved. Furthermore, another type of intermittency observed via pointwise characterizations is the switching between either acoustic or hydrodynamic modes. In contrast, the present situation indicates that the time dependent pressure signal and the average spectra represent a single locked-on state, whereas the instantaneous, global flow pattern can exhibit occasional departures.

Fig. 7b shows the results of averaging: (a) phase-locked images, one of which is shown in the top image of Fig. 7a; and (b) non-phase-locked images, two of which are shown in the bottom and middle images of Fig. 7a. The top image corresponds to a phase-average of eleven instantaneous images from the phase-locked set. The second image is obtained from an average of the top image with one non-phase-locked image from the left and right sidebands, which are represented by the types of patterns of vorticity shown in the middle and bottom images of Fig. 7a. The third image of Fig. 7b includes two non-phase-locked instantaneous images from the left and right sidebands and the bottom image of Fig. 7b includes three non-phase-locked images from each of the sidebands. It is therefore evident that phase averaging strictly on the basis of a reference signal in the pipeline-cavity system can lead to distorted representations, at least for low levels of the self-excited acoustic signal characteristic of the present configuration, described in Section 2.4.

8. Concluding remarks

Flow tones arising from separated flow along a cavity configuration have been the subject of a wide variety of investigations over the past few decades. Typical experimental approaches have provided pressure and velocity at selected points. The present study provides the first instantaneous global representations of flow-acoustic coupling using a technique of high-image-density particle image velocimetry. This approach reveals the instantaneous flow patterns due to the instability of a fully turbulent inflow along a cavity and its coupling with the resonant modes of the pipeline-cavity system.

The major physical features addressed herein are: (i) the onset of vortex formation in the separated shear layer along the cavity; (ii) the hydrodynamic contribution of the separated layer to the acoustic power generation; (iii) the intermittent occurrence of locked-on states of vortex formation in the shear layer; and finally, (iv) the averaged patterns of the flow, which show the relationship between the shear layer along the cavity and the recirculation cell within the cavity. All of these features form a basis for understanding the origin of tone generation.

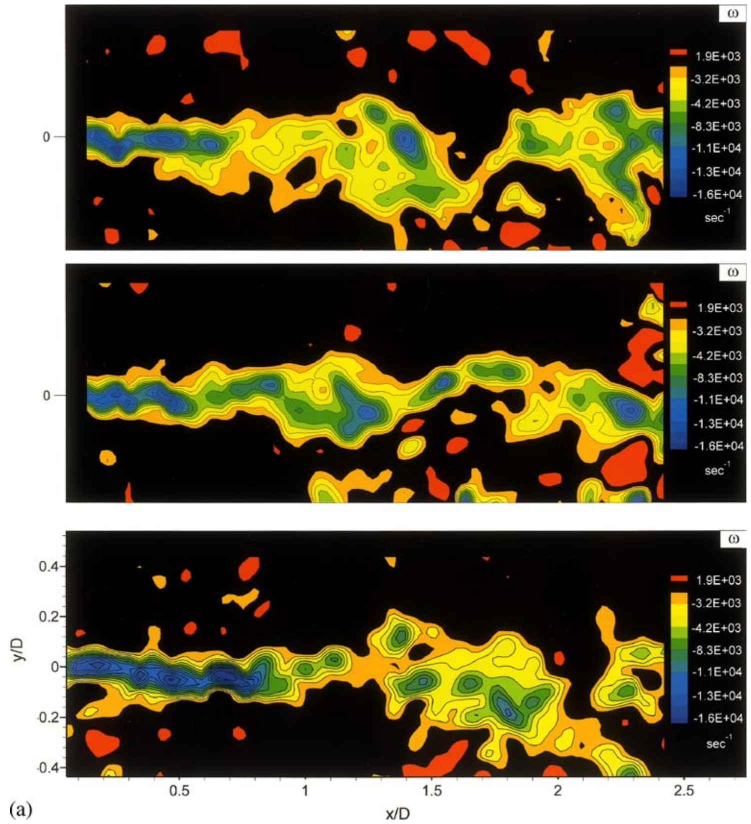

Fig. 7. (a) Representative instantaneous images that show the nature of non-phase-locked formation of large-scale clusters of vorticity. Top image is from the phase-locked sequence, middle image is from the left sideband and bottom image is from the right sideband of the non-phase-locked images. In all images, the minimum contour level is $-16{,}000\,\mathrm{s}^{-1}$ and the increment is $1280\,\mathrm{s}^{-1}$. The first two levels above and below zero are omitted for clearer illustration of the flow structure. (b) Effect of including sideband images on calculation of the phase-averaged image. The first image shows the original phase-average, which is based only on phase-locked, instantaneous images. The second image is a phase-average based on the same instantaneous images used for the phase-average of the first (top) image, but including one non-phase-locked image from the right sideband and one from the left sideband. The third image includes two non-phase-locked images from each sideband, and the fourth image includes three non-phase-locked images from each sideband.

8.1. Vortex formation in the shear layer along the cavity

It is generally acknowledged, on the basis of qualitative flow visualization and theoretical/numerical approaches, that the occurrence of flow tones is associated with the formation of identifiable vortices in the shear layer along the cavity, provided the cavity is sufficiently long. The frequency of formation of such vortices is directly related to the frequency of the flow tone. Moreover, such vortices contribute to the generation of acoustic power. To date, the quantitative structure of vortex formation has received relatively little attention, especially for the case of a fully turbulent inflow in the presence of a resonant acoustic mode that is nominally aligned with the direction of the inflow. The principal results of the present study are described in the following.

8.1.1. Onset of organized vortices from fully turbulent inflow

Despite the fact that the inflow to the cavity is fully turbulent, large-scale vortices form in the shear layer along the cavity. This organized vortex structure occurs even though the cavity is relatively shallow. That is, the development and propagation of the large-scale vortices appear to be relatively unaffected by confinement effects. This observation provides the physical explanation for a constant value of Strouhal number fD/U, over a range of cavity depth W/D, of the unsteady pressure fluctuations characterized by Rockwell et al. (2003).

It is remarkable that these large-scale vortical structures occur for a relatively low value of the self-excited acoustic velocity fluctuation u_a relative to the centerline velocity U of the inflow, i.e., of $u_a/U \sim 10^{-2}$. It should be emphasized

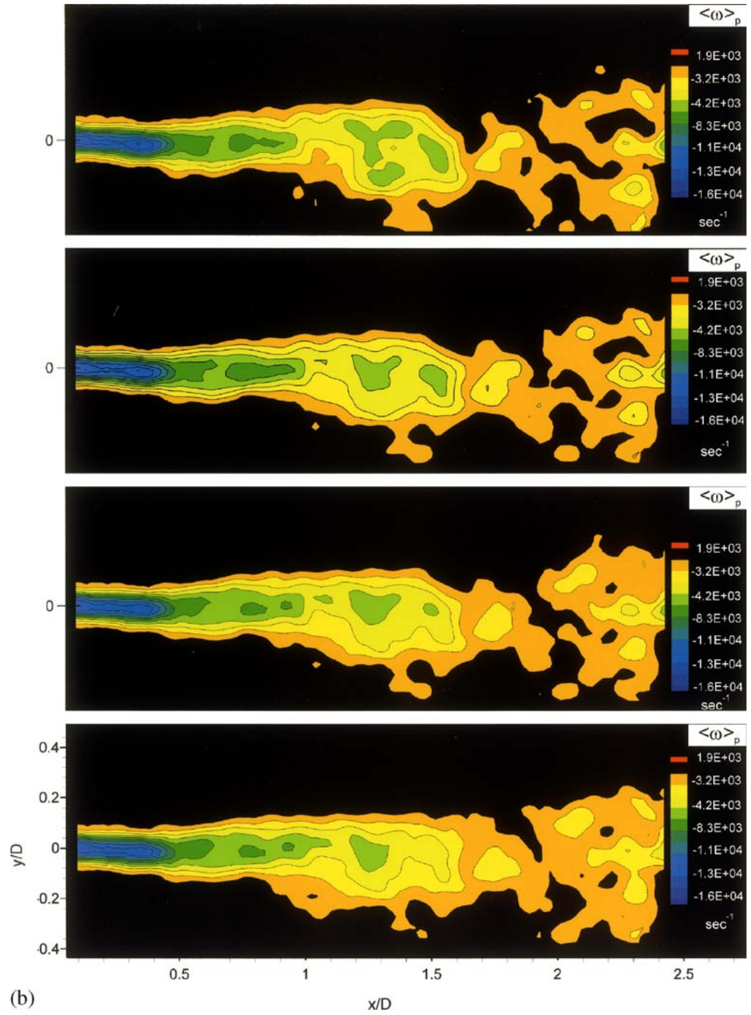

Fig. 7 (*continued*).

that, in the present case of a fully turbulent boundary layer at the nozzle exit, it is necessary to overcome the effects of broadband turbulence during the process of generation of highly organized, large-scale vortical structures. This situation contrasts with previous related investigations, which typically have involved accelerated laminar, transitional or undocumented boundary layers at the location of separation. Associated with this relatively low value of u_a/U, however, are the observations that the large-scale vortices develop over a relatively long streamwise distance from the leading-corner of the cavity, and the vorticity of a given large-scale vortex is broadly distributed. This situation contrasts, for example, with the rapid onset of large-scale vortices immediately downstream of an orifice plate in the presence of a resonant acoustic field.

8.1.2. *Route to formation of large-scale vortices*

The development of the shear layer leading to large-scale vortex formation is unlike the classical roll-up of a laminar, separated shear layer. Even though the inflow is fully turbulent, highly coherent and concentrated small-scale vortices are formed abruptly from the leading-corner of the cavity, due to a large gradient of vorticity at the corner. As a result, the initial region of the separated layer is dominated by a train of sequential, small-scale vortices. They eventually roll up to form a large-scale vortical structure, which has broadly distributed vorticity. The dimensionless circulation Γ^* of these small-scale vortices is less than an order of magnitude smaller than the value of Γ^* for the large-scale vortex, yet they produce locally significant contributions to the instantaneous acoustic power generation, as outlined in Section 8.2.

8.1.3. Phase speed and wavelength of large-scale vortices as a basis for a kinematic model

The well-known equation for the dimensionless frequency of flow tone generation is: $fL/U = c_v/U(n+a)$, in which L is the cavity length, U is the freestream velocity of the inflow, c_v is the phase speed of the vortex (or equivalently the instability wave), n is the stage number, and a is the end correction. From an experimental standpoint, the major share of investigations to date have arbitrarily selected values of c_v/U and a to provide suitable fits of measured values of fL/U. Using the technique of quantitative imaging described herein, it is possible to determine independently values of c_v/U, n, and a, for cases where large-scale vortices are formed. Values of $c_v/U \cong 0.5$, $n = 2$, and $a = 0.5$ clearly demonstrate that the highly locked-on formation of large-scale vortices is due to the second ($n = 2$) stage of oscillation. It is emphasized, however, that this direct link between the physics of the vortex development and the aforementioned kinematic equation for fL/U is valid only in downstream regions of the cavity where concentrations of vorticity and contours of constant vertical velocity fluctuation of the shear layer are well-defined. The initial region of the shear layer development from the leading-corner of the cavity may be associated with streamwise variations of wavelength $\lambda = c_v/f$. It is unlikely that a single value of a will be universal for the range of length L and depth W of the cavity.

8.2. Acoustic power generation due to the shear layer along the cavity

In order for a flow tone to persist, adequate acoustic power must be generated. The principal contributions to the acoustic power are from vorticity $\boldsymbol{\omega}$, velocity $\boldsymbol{V}$, and acoustic particle velocity $\boldsymbol{u}_a$, according to the integral of Eq. (1). If all of the vorticity in the shear layer is assumed to be confined to the vortex of circulation Γ^* and the scale of the vortex is much smaller than the acoustic wavelength, then the integral for the acoustic power generation by the vortex is simplified to $P \cong \rho\Gamma^* \boldsymbol{k} \cdot (\boldsymbol{V} \times \boldsymbol{u}_a)$, in which $\boldsymbol{k}$ is a unit vector, and $\boldsymbol{V}$ and $\boldsymbol{u}_a$ are evaluated at the center of the vortex. As described in the references cited in the Introduction, the generation of acoustic power P is often described in terms of an isolated, experimentally visualized vortex, or a single concentrated vortex of circulation Γ^*, its velocity $\boldsymbol{V}_v$ and the acoustic particle velocity $\boldsymbol{u}_a$. In most works, the acoustic resonator is a side branch, and the pattern of the acoustic particle velocity $\boldsymbol{u}_a$ is well defined. The vortex may show substantial variations of the vertical velocity component $(V_v)_y$ along its trajectory during an oscillation cycle.

In contrast to the foregoing, the distinctive feature of the large-scale vortex in the present study is that its vorticity is broadly distributed, due to the manner in which it is generated, as described in Section 8.1.2. Moreover, its trajectory is predominantly in the horizontal direction, such that $(V_v)_y \cong 0$. A further, important point is that the large-scale vortices contain only a fraction of the vorticity ω_z in the separated shear layer, and it is therefore necessary to account for the entire layer of ω_z along the cavity when calculating the acoustic power.

8.2.1. Vorticity layer near the leading-corner of the cavity

Near the leading-corner of the cavity, the magnitude of the instantaneous vorticity ω_z is very large due to the steep slope of the turbulent boundary layer at separation. The instantaneous hydrodynamic contribution to the power integral (see Eq. (1)), which is defined as $\boldsymbol{\omega} \times \boldsymbol{V} = \boldsymbol{k}\omega_z \times \boldsymbol{V}$, takes on very large values immediately downstream of the leading-corner of the cavity. These vectors are predominantly oriented in the vertical direction. In the vicinity of the leading-corner of the cavity, the pattern of the acoustic velocity field $\boldsymbol{u}_a$ will be distorted significantly from its nominally horizontal orientation. As a consequence, this region represents a significant contribution to the magnitude of the instantaneous acoustic power P.

8.2.2. Vorticity within large-scale vortex

The distributed vorticity within the large-scale vortex yields significant horizontal and vertical contributions to the instantaneous hydrodynamic component $\boldsymbol{\omega} \times \boldsymbol{V} = \boldsymbol{k}\omega_z \times \boldsymbol{V}$ of the acoustic power integral. Near the central region of the cavity, where large-scale vortices have formed, the hydrodynamic component $[\boldsymbol{\omega} \times \boldsymbol{V}]_x$ in the horizontal direction shows adjacent positive and negative regions. On the other hand, the hydrodynamic component $[\boldsymbol{\omega} \times \boldsymbol{V}]_y$ in the vertical direction shows significant levels of the same sign along the entire shear layer. The acoustic particle velocity $\boldsymbol{u}_a$ will have a horizontal component $[\boldsymbol{u}_a]_x$ along the entire extent of the shear layer, and midway along the cavity, only the component $[\boldsymbol{u}_a]_x$ will exist. Close to the trailing-corner of the cavity, distortion of the acoustic velocity that is nominally oriented in the axial direction will produce a vertical component $[\boldsymbol{u}_a]_y$. Therefore the potential exists for alignment of both of the instantaneous components $[\boldsymbol{\omega} \times \boldsymbol{V}]_x$ and $[\boldsymbol{\omega} \times \boldsymbol{V}]_y$ with the corresponding projections of the acoustic velocity field as the large-scale vortex moves along the cavity. Regarding the alignment between $[\boldsymbol{u}_a]_x$ and $[\boldsymbol{\omega} \times \boldsymbol{V}]_x$, even if it does occur, the possibility of cancellation effects due to the aforementioned adjacent positive and negative regions of $[\boldsymbol{\omega} \times \boldsymbol{V}]_x$ will tend to yield a small or zero net contribution to the acoustic power.

An additional consideration is the magnitude of $[\boldsymbol{\omega} \times \boldsymbol{V}]_y$, relative to the magnitude of $[\boldsymbol{\omega} \times \boldsymbol{V}]_x$. Comparison of the peak values of $[\boldsymbol{\omega} \times \boldsymbol{V}]_y$ and $[\boldsymbol{\omega} \times \boldsymbol{V}]_x$, as defined in the foregoing Sections 8.2.1 and 8.2.2, shows that the peak value of the former substantially exceeds the latter, due to the very high gradient of vorticity of the separating turbulent boundary layer near the leading-corner of the cavity.

8.2.3. Vorticity and hydrodynamic contribution to acoustic power: recommendations for implementation

Considering together the points raised in the previous parts of Section 8.2, including Sections 8.2.1 and 8.2.2, it is intended that this type of detailed description of the hydrodynamic field during flow-acoustic coupling can provide guidance for numerical simulations that, first of all, must effectively compute patterns of velocity and vorticity then, as a more stringent requirement, determine patterns of the hydrodynamic contribution $\boldsymbol{\omega} \times \boldsymbol{V}$ to the acoustic power integral, as well as its projections in the x and y directions. When these essential components of Howe's acoustic power integral are properly simulated, then it should be possible to proceed to a complete evaluation of the generated acoustic power, fully accounting for the acoustic field, which has not been addressed in the present investigation. In the spirit of the original formulation of this integral, the acoustic field can be computed independently, provided the oscillation amplitude is not excessively high, as is the case for the present experiments.

8.3. Intermittency of locked-on states of vortex formation in shear layer along cavity

The acquisition of instantaneous images was phase-referenced to the instantaneous pressure signal in the pipe resonator. This approach is different from the traditional one based on time- or phase-averaged representations of pressure and velocity at defined points. The imaging technique shows that even though the unsteady pressure fluctuation in the acoustic resonator is highly periodic and persistent, the patterns of flow structure, e.g., vorticity, are not necessarily repeatable for all images acquired at a given phase of the pressure fluctuation. A well-defined, predominant state of the flow pattern may be taken to represent the locked-on state. It is evident, however, that deviations, or sidebands, of flow patterns occur about the locked-on flow pattern. The consequence of this previously unreported phenomenon is that, if phase-averaging is employed strictly on the basis of a reference signal in the resonator, representations of the flow structure will be smoothed, i.e., distorted, in relation to the representation based solely on occurrences of purely locked-on states of the flow.

From a physical standpoint, a pipeline-cavity resonator is lightly damped, and when non-locked-on states of the flow occur, the resonator response is relatively unaffected, since a large number of cycles of oscillation are required for the resonator response to decay significantly. It should be emphasized that this phenomenon is most likely limited to cases where the acoustic particle velocity u_a is very small in relation to the characteristic velocity of the mean flow U; for the present study, $u_a/U \sim 10^{-2}$. In the limiting case, where a consistent non-locked-on state occurs, which was not observed in this investigation, the occurrence of absorption of sound energy should attenuate the amplitude of the acoustically–coupled resonance.

For other types of resonator configurations, e.g., a lightly damped side branch, the acoustic amplitudes can be much larger, and one can anticipate highly consistent, phase-repetitive flow structure from one cycle to the next.

8.4. Averaged patterns of flow: role and structure of recirculation cell in the cavity

Time-averaged images of streamline patterns, root-mean-square fluctuations, and Reynolds stresses yield a composite view of the separated shear-layer along the cavity and the recirculation zone within the cavity. The time-averaged streamline pattern shows a single recirculation cell centered near the downstream corner of the cavity, rather than a single cell centered within the cavity. Furthermore, this type of streamline pattern involving a corner cell is associated with two distinct, adjacent layers of Reynolds stress upstream of the trailing-corner of the cavity.

The time-averaged vorticity in the separating shear layer has very high values at the leading-corner of the cavity and rapidly decays with downstream distance. The development of the large-scale vortex along this layer of high time-averaged vorticity is a central feature of the unsteady flow field, as described in the aforementioned sections. On the other hand, the time-averaged vorticity is relatively low within the cavity, except near the region of the recirculation cell. This finding indicates that the recirculation region within the cavity, except the region near the downstream corner, is not a significant source of acoustic power, since the hydrodynamic contribution to the power at any location requires a significant level of vorticity.

References

Blake, W.K., 1986. Mechanics of Flow-Induced Sound and Vibration, Vols. 1 and 2. Academic Press, New York.
Bruggeman, J.C., 1987. Flow-Induced Pulsations in Pipe Systems, Doctoral Dissertation. Technical University of Eindhoven.

Bruggeman, J.C., Hirschberg, A., Van Dongen, M.E.H., Wijnands, A.P.J., Gorter, J., 1989. Flow induced pulsations in gas transport systems: analysis of the influence of closed side branches. Journal of Fluids Engineering 111, 484–491.

Bruggeman, J.C., Hirschberg, A., Van Dongen, M.E.H., Wijnands, A.P.J., Gorter, J., 1991. Self-sustained aero-acoustic pulsations in gas transport systems: experimental study of the influence of closed side branches. Journal of Sound and Vibration 150, 371–393.

Cremer, L., Ising, H., 1967. Die selbsterregten schwingungen von orgelpfeifen. Acustica 19, 143–153.

Demetz, F.C., Farabee, T.M., 1977. Laminar and turbulent shear flow-induced resonances. AIAA Paper 77-1293.

Elder, S.A., 1978. Self-excited depth-mode resonance for a wall-mounted cavity in turbulent flow. Journal of Acoustical Society of America 64, 877–890.

Elder, S.A., Farabee, T.M., Demetz, F.C., 1982. Mechanisms of flow-excited cavity tones at low Mach number. Journal of Acoustical Society of America 72, 532–549.

Green, R.B., Gerrard, J.H., 1993. Vorticity measurements in the near-wake of a circular cylinder at low Reynolds number. Journal of Fluid Mechanics 246, 675–691.

Hofmans, G.C.J., 1998. Vortex Sound in Confined Flows, Doctoral Dissertation. Technical University of Eindhoven.

Hourigan, K., Welsh, M.C., Thompson, M.C., Stokes, A.N., 1990. Aerodynamic sources of acoustic resonance in a duct with baffles. Journal of Fluids and Structures 4, 345–370.

Howe, M.S., 1975. Contributions to the theory of aerodynamic sound, with application to excess jet noise and theory of the flute. Journal of Fluid Mechanics 71, 625–673.

Howe, M.S., 1980. The dissipation of sound at an edge. Journal of Sound and Vibration 70, 407–411.

Howe, M.S., 1997. Edge, cavity and aperture tones at very low Mach numbers. Journal of Fluid Mechanics 330, 61–84.

Howe, M.S., 1998. Acoustics of Fluid–Structure Interaction. Cambridge University Press, Cambridge.

Huang, X.Y., Weaver, D.S., 1991. On the active control of shear layer oscillations across a cavity in the presence of pipeline acoustic resonance. Journal of Fluids and Structures 5, 207–219.

Kriesels, P.C., Peters, M.C.A.M., Hirschberg, A., Wijnands, A.P.J., Iafrati, A., Riccaradi, G., Piva, R., Bruggeman, J.-C., 1995. High amplitude vortex-induced pulsations in a gas transport system. Journal of Sound and Vibration 184, 343–368.

Landreth, C.C., Adrian, R.J., 1989. Measurement and refinement of velocity data using high-image-density analysis in particle image velocimetry. In: Adrian, R., Asanuma, T., Durão, D., Durst, F., Whitelaw, J. (Eds.), Applications of Laser Anemometry to Fluid Mechanics. Springer, New York, pp. 484–497.

Lin, J.-C., Rockwell, D., 2001a. Oscillations of a turbulent jet incident upon an edge. Journal of Fluids and Structures 15 (6), 791–829.

Lin, J.-C., Rockwell, D., 2001b. Organized oscillations of an initially turbulent flow past a cavity. AIAA Journal 39 (6), 1139–1151.

Monkewitz, P.A., Huerre, P., 1982. Influence of the velocity ratio on the spatial instability of mixing layers. Physics of Fluids 25 (7), 1137–1143.

Nelson, P.A., Halliwell, N.A., Doak, P.E., 1981. Fluid dynamics of a flow excited resonance. Part I: Experiment. Journal of Sound and Vibration 78, 15–38.

Nelson, P.A., Halliwell, N., Doak, P.E., 1983. Fluid dynamics of a flow excited resonance, Part II: Flow acoustic interaction. The dissipation of sound at an edge. Journal of Sound and Vibration 91, 375–402.

Pereira, J.C.F., Sousa, J.M.M., 1995. Experimental and numerical investigation of flow oscillations in a rectangular cavity. Journal of Fluids Engineering 117, 68–74.

Pollack, M.L., 1980. Flow-induced tones in side-branch pipe resonators. Journal of the Acoustical Society of America 7, 1153–1156.

Radavich, P.M., Selamet, A., Novak, J.M., 1999. Acoustic source location in flow-excited quarter wave resonators. Internoise 99, Fort Lauderdale, FL, December, 6–8, pp. 341–346.

Rockwell, D., 1983. Oscillations of impinging shear layers. Invited Lecture, 20th Aerospace Sciences Meeting of AIAA, January, 1981, Orlando, FL; AIAA Paper 81-0047 (also see AIAA Journal 21, 645–664).

Rockwell, D., 1998. Vortex–body interactions. Annual Review of Fluid Mechanics 30, 199–229.

Rockwell, D., Naudascher, E., 1978. Review—self-sustaining oscillations of flow past cavities. Journal of Fluids Engineering 100, 152–165.

Rockwell, D., Naudascher, E., 1979. Self-sustained oscillations of impinging free-shear layers. Annual Review of Fluid Mechanics 11, 67–94.

Rockwell, D., Schachenmann, A., 1982a. Self-generation of organized waves in an impinging turbulent jet at low Mach number. Journal of Fluid Mechanics 117, 425–441.

Rockwell, D., Schachenmann, A., 1982b. The organized shear layer due to oscillations of a turbulent jet through an axisymmetric cavity. Journal of Sound and Vibration 85, 371–382.

Rockwell, D., Lin, J.-C., Oshkai, P., Reiss, M., Pollack, M., 2003. Shallow cavity flow tone experiments: Onset of locked-on states. Journal of Fluid and Structures 17 (3), 381–414.

Schachenmann, A., Rockwell, D., 1980. A quasi-standing-wave phenomenon due to oscillating internal flow. Journal of Fluids Engineering 102, 70–77.

Stoubos, A.K., Benocci, C., Palli, E., Stoubos, G.K., Olivari, D., 1999. Aerodynamically generated acoustic resonance in a pipe with annular flow restrictors. Journal of Fluids and Structures 13, 755–778.

Takakura, Y., Higashino, F., Yoshizawa, T., Ogawa, S., 1996. Numerical study on unsteady supersonic cavity flows. AIAA Paper 96-2092.

Ziada, S., 1994. A flow visualization study of flow-acoustic coupling at the mouth of a resonant side-branch. Journal of Fluids and Structures 8, 391–416.

Ziada, S., Bühlman, E.T., 1992. Self-excited resonances of two-side-branches in close proximity. Journal of Fluids and Structures 6, 583–601.

Ziada, S., Shine, S., 1999. Strouhal numbers of flow-excited acoustic resonance of closed side branches. Journal of Fluids and Structures 13, 127–142.

Zoccola Jr., B.J., 2000. Experimental Investigation of Flow-Induced Cavity Resonance, Naval Surface Warfare Center, NSWCCD-TR-2000/010 (June), Carderock Division, West Bethesda, MD 20817-5700.